

EFFECTS OF ELECTROLYTE COMPOSITION AND POLYSULFIDE SPECIES ON  
THE REACTIVITY OF LITHIUM ANODES IN LITHIUM-SULFUR BATTERIES

A Thesis

by

TAYLOR WILLIAM SMITH

Submitted to the Office of Graduate and Professional Studies of  
Texas A&M University  
in partial fulfillment of the requirements for the degree of  
MASTER OF SCIENCE

Chair of Committee,	Perla B. Balbuena
Committee Members,	Partha P. Mukherjee
	Patrick J. Shamberger
Head of Department,	Ibrahim Karaman

December 2015

Major Subject: Materials Science and Engineering

Copyright 2015 Taylor W. Smith

## ABSTRACT

In attempting to develop energy storage systems possessing superior properties to traditional lithium ion batteries (LIBs), numerous alternative chemistries have undergone study and development. Of these, the lithium-sulfur battery seems one of the more promising contenders for replacing LIBs, particularly for applications like electric vehicles. Nevertheless, a variety of limitations have prevented lithium-sulfur battery introduction to the marketplace, in spite of almost fifty years of research, including polysulfide shuttle, reactivity of the electrolyte, and anodic microstructure evolution. This thesis will explore the use of first-principles computational techniques in understanding the impact of electrolyte composition, polysulfide molecules, and lithium crystal structure on the reactions taking place near the lithium anode in order to better address the problems facing lithium-sulfur batteries. Using ab initio molecular dynamics simulations (AIMD), in conjunction with static density functional theory (DFT) optimizations, Bader charge analysis, and additional analytical techniques, the interactions and impacts of the different components of the typical lithium-sulfur battery can be examined on a molecular basis. It is the author's hope that a better theoretical understanding of how these species behave will enable design and implementation of real-world lithium-sulfur systems capable of meeting and overcoming the difficulties facing their commercialization.

In order to test the effects of lithium crystal structure on electrolyte stability and surface morphology evolution, both a (100) and (110) lithium metal surface were created

and tested using AIMD simulations. There was a minimal difference in the results for each structure, in both the surface morphology and ratio of solvent molecules reduced by the lithium. In testing the effects and stability of various solvents, it was found that ethylene carbonate reduced readily, while dioxolane, dimethoxyethane, and fluorinated ether molecules were quite stable in the presence of the anode. AIMD simulations of polysulfide molecules in the vicinity of the lithium surface show high reactivity, as seen experimentally, and subsequent DFT calculations indicate the reduction of long-chain polysulfide molecules in the presence of Li atoms is a thermodynamically favorable reaction pathway. Finally, it was observed that high molarity salt systems have properties capable of improving cell performance.

## DEDICATION

This thesis is dedicated first and foremost to my lovely wife, Rachel, for putting up with 2.5 years of Texas and even more of me. Thank you for your unconditional love and support. Also dedicated to my loving family and friends, for the encouragement and instruction you've given me over the years. Finally, I dedicate this thesis to those who will in all likelihood never see it; the children, the burned-out, the confused and scared. There may be nothing here for you but a message: that you *can* dream big, you *can* make something out of yourself, you *can* change the world, no matter who you are or where you come from. Nothing earth-shattering is found in these pages, save for the author's journey into adulthood and the professional realm. I didn't change the world, as I had set out to, just my own. And now *I will make this world of my devising.*

## ACKNOWLEDGEMENTS

I would like to thank my committee chair, Dr. Balbuena, for all the support, encouragement, and instruction she has given me, and for allowing me to work with her and learn from her for the past year. It has truly been a privilege, and her mentorship has most certainly made me a better researcher and person. I would also like to thank my other committee members, Dr. Mukherjee and Dr. Shamberger, for agreeing to sift through roughly 100 pages of thesis and the subsequent defense presentation, as well as for your support and guidance in this process.

Thank you to the staff and professors of the Artie McFerrin Department of Chemical Engineering, for giving me the opportunity to become a graduate student at Texas A&M, and for my colleagues in the department, for helping me survive that brutal first semester and continuing to share your support and encouragement. Thank you to the Department of Materials Science and Engineering, for taking me in and teaching me so much in such a short amount of time. Thank you to the TAMU Supercomputing Facility and their HPC systems for allowing me to (somewhat) smoothly perform my research. And thank you to Luis Camacho Forero, my colleague and office-mate, for helping me learn how to conduct computational research, and for answering my many, many questions.

## TABLE OF CONTENTS

	Page
ABSTRACT.....	ii
DEDICATION.....	iv
ACKNOWLEDGEMENTS.....	v
TABLE OF CONTENTS.....	vi
LIST OF FIGURES.....	vii
LIST OF TABLES.....	x
CHAPTER I INTRODUCTION.....	1
Literature Review.....	1
Methodology.....	8
CHAPTER II EFFECTS OF LITHIUM SURFACE STRUCTURE.....	13
CHAPTER III EFFECTS OF ELECTROLYTE COMPOSITION.....	25
Salt.....	25
Polysulfides.....	35
D2.....	56
LiFSI.....	59
CHAPTER IV HIGH MOLARITY SALT EFFECTS.....	65
CHAPTER V SUMMARY.....	84
REFERENCES.....	87

## LIST OF FIGURES

		Page
Figure 1	Typical Li-ion cell.....	1
Figure 2	Uniform lithium expansion of a host matrix.....	2
Figure 3	Li-Si thin film electrode after electrochemical cycling.....	3
Figure 4	Traditional Li-S battery.....	5
Figure 5	DOL/DME, 1 M LiTFSI system .....	12
Figure 6	EC/DME, (100) at 0 ps .....	15
Figure 7	EC/DME, (110) at 0 ps .....	16
Figure 8	EC/DOL, (100) at 0 ps .....	17
Figure 9	EC/DOL, (110) at 0 ps .....	19
Figure 10	DOL/DME, (100) at 0 ps .....	20
Figure 11	DOL/DME, (110) at 0 ps .....	21
Figure 12	Summary of solvent reactivity results for (100) and (110) crystals.....	22
Figure 13	Left: EC/DME, 1M LiTFSI at 0ps .....	27
Figure 14	CF <sub>3</sub> group leaving .....	28
Figure 15	Salt at the end of EC/DME simulation .....	29
Figure 16	C <sub>2</sub> O <sub>2</sub> H <sub>4</sub> near the lithium surface .....	30
Figure 17	Left: EC/DOL, 1M LiTFSI at 0ps .....	31
Figure 18	Salt configuration in EC/DOL at 1 ps .....	32
Figure 19	SO <sub>2</sub> group at the anode surface at 5.2 ps .....	33
Figure 20	Lithium, nitrogen, sulfur interaction at the anode surface .....	33

Figure 21	Left: DOL/DME, 1M LiTFSI at 0ps .....	34
Figure 22	DOL/DME, 1M LiTFSI, 1M PS at 0ps .....	42
Figure 23	Left: DOL/DME, 1M LiTFSI, 1M PS at 100 fs .....	43
Figure 24	DOL/DME, 1M LiTFSI, 2M PS at 0ps .....	45
Figure 25	Left: DOL/DME, 1M LiTFSI, 2M PS at 500 fs .....	46
Figure 26	DOL/DME, 1M LiTFSI, 2M PS at 2.3 ps .....	48
Figure 27	Left: DOL/DME, 1M LiTFSI at 9.2 ps.....	49
Figure 28	DOL/DME, 1M LiTFSI, 3M PS at 0ps .....	50
Figure 29	Left: DOL/DME, 1M LiTFSI, 3M PS at 9.8 ps .....	51
Figure 30	Ring configuration of $\text{Li}_2\text{S}_8$ .....	53
Figure 31	DOL/DME, 1M LiTFSI, 3M PS at 0 ps .....	54
Figure 32	DOL/DME, 1M LiTFSI, 3M PS at 12.3 ps .....	55
Figure 33	DOL/D2, 1M LiTFSI, 1M PS at 0ps .....	57
Figure 34	Left: DOL/D2, 1M LiTFSI, 1M PS at 0 ps.....	58
Figure 35	Left: DME, 1M LiFSI, at 0 ps .....	60
Figure 36	Left: DME, 1M LiTFSI, at 0 ps .....	61
Figure 37	LiFSI molecule in DME at 16 ps, and after the addition of one extra electron .....	63
Figure 38	Left: DME, 4M LiTFSI, at 0 ps .....	66
Figure 39	Left: DME, 4M LiFSI, at 0 ps .....	67
Figure 40	Charge analysis results for molecule 1.....	69
Figure 41	Left: DME, 4M LiFSI, at 200 fs, highlighting molecule 1 .....	70
Figure 42	Left: DME, 4M LiFSI, at 1.9 ps, highlighting molecule 1.....	71



Figure 43	Charge analysis results for molecule 2 .....	72
Figure 44	Left: DME, 4M LiFSI, at 1.9 ps, highlighting molecule 2 .....	73
Figure 45	Charge analysis results for molecule 3 .....	74
Figure 46	Left: DME, 4M LiFSI, at.9.0 ps, highlighting molecule 3 .....	75
Figure 47	Charge analysis results for molecule 4 .....	76
Figure 48	DME, 4M LiFSI, at.16.0 ps, highlighting molecule 4.....	77
Figure 49	Direction of lithium attack .....	79
Figure 50	Reaction energies at various lithium orientations .....	80
Figure 51	Optimized structure of below Li <sup>0</sup> attack .....	81

## LIST OF TABLES

	Page
Table 1 List of electrolyte component properties .....	11
Table 2 PS bond dissociation energies obtained from B3PW91/6-311++G(p,d) calculations.....	37
Table 3 LiTFSI energy of dissociation in gas-phase and DME .....	63
Table 4 LiFSI energy of dissociation in gas-phase and DME .....	64
Table 5 LiF formation energetics .....	81

# CHAPTER I

## INTRODUCTION

### Literature Review

Over the past four decades, lithium-ion batteries (LIBs) have become ubiquitous in portable electronics and the public conscience. They are the primary power source for the cameras, cell phones, laptops, and other gadgets that allow our modern world to function every day. Beyond this, the technology has the potential to make hybrid electric vehicles (HEVs) an economically viable mode of transportation.<sup>1</sup> In order for this to happen, though, both the lifetime and capacity of the battery electrodes must be improved.<sup>2</sup> Figure 1 (below) shows the setup for a traditional lithium battery system. Traditionally the cathode consists of a lithium metal oxide compound (such as  $\text{LiCoO}_2$ ), while the anode is typically made of graphite.

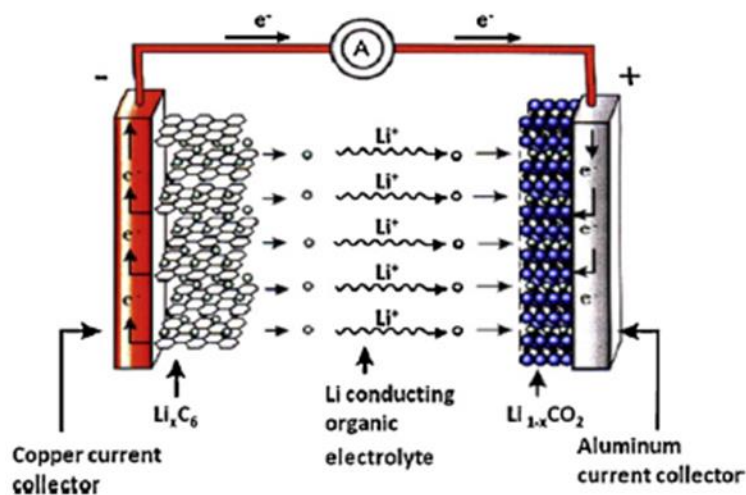
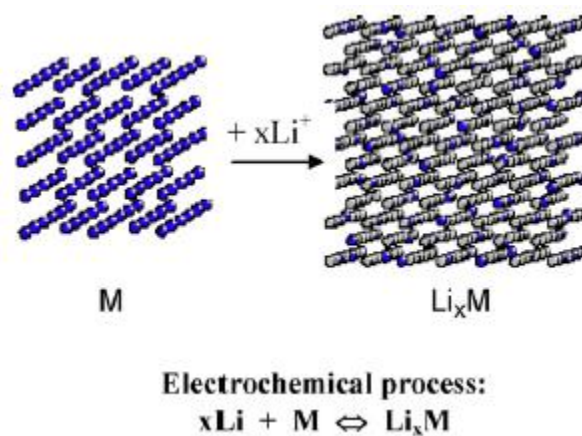


Figure 1. Typical Li-ion cell<sup>3</sup>

At the electrodes, the chemo-mechanical effects associated with lithium intercalation/de-intercalation directly impact the cell performance and involve interactions between a variety of mechanisms, including diffusion, plastic flow, chemical reactions, and the evolution of material properties.<sup>4</sup> Deformation induced by insertion, as illustrated in Figure 2, fundamentally limits the materials and structures practical for battery electrodes. For certain chemistries, nearly 100% of the available lithium ions are extracted or inserted upon charge or discharge, leading to massive changes in volume.



**Figure 2.** Uniform lithium expansion of a host matrix

For instance, in lithium manganese oxide cathodes ( $\text{LiMn}_2\text{O}_4$ ), lithium depletion to 20% of the stoichiometric value reduces electrode volume by 6.5%.<sup>5</sup> This effect becomes much more problematic during fast charging, as the surface of the material delithiates first, resulting in a large tensile hoop stress during the shrinkage of the outer

layer. The stress can create cracks, cause them to propagate, and can even lead to comminution of the oxide particles. Similar effects can also be seen in the anode. In the case of the graphite anode used in traditional LIBs, every six carbon atoms accommodates 0.6 lithium atoms, resulting in a volume expansion of around 8% for full lithiation.<sup>6</sup> For higher capacity chemistries the effects are much more pronounced. For instance, in lithium-silicon cells, each silicon atom can accommodate up to 4.4 lithium atoms upon full lithiation, yielding a volume change of over 300%.<sup>7</sup> If the electrode material is mechanically constrained due to a current collector (for instance, a conductive substrate) or binder (used to hold the active particles in the electrode in place), large stresses will develop upon electrochemical cycling. Ultimately, this can generate cracks in the electrode material, as can be seen in the thin-film lithium-silicon electrode (Figure 3) seen below.

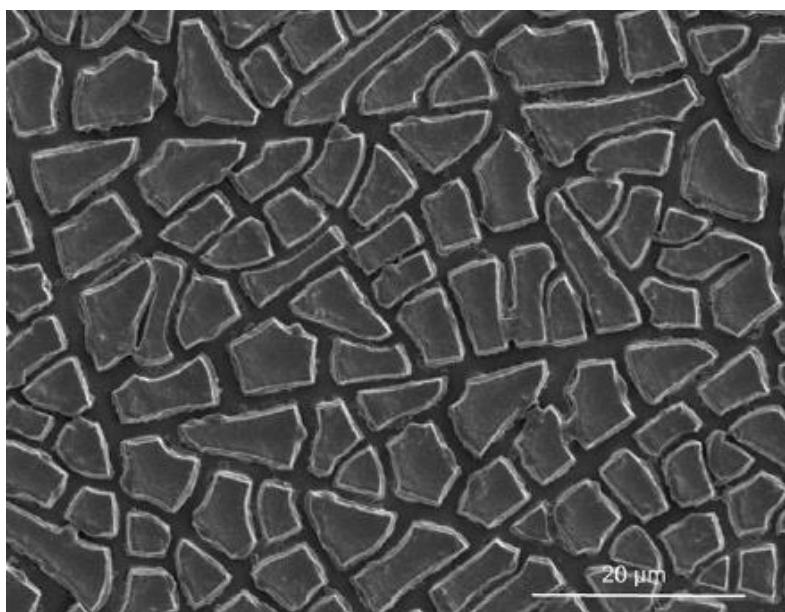


**Figure 3.** Li-Si thin film electrode after electrochemical cycling<sup>8</sup>

Even in the case where there are no mechanical constraints on the system, lithium concentration inhomogeneity caused by finite diffusivity of lithium can result in stresses. A stress that arises because of inhomogeneity of composition during transport in solid materials via diffusion occurs in many different scientific disciplines and is typically referred to as diffusion-induced stress (DIS).

These chemo-mechanical considerations, among other factors, are a fundamental limitation to battery performance, and while the specific energy of LIBs has been significantly increased within the last two decades due to advances in battery engineering, further increases will only be possible by utilizing alternative electrode designs and chemistries, ideally ones which either accommodate these stress effects or eliminate them. Thus, systems involving pure lithium anodes (such as lithium-air and lithium-sulfur batteries) are ideal for eliminating these concerns. In particular, Li-S batteries possess many favorable characteristics that make them an attractive alternative to current lithium ion technology. Their high theoretical specific capacity and energy density allow for up to double the gravimetric energy density of conventional Li-ion systems, in addition to being extremely cost-effective. A typical Li-S cell is shown below in Figure 4.

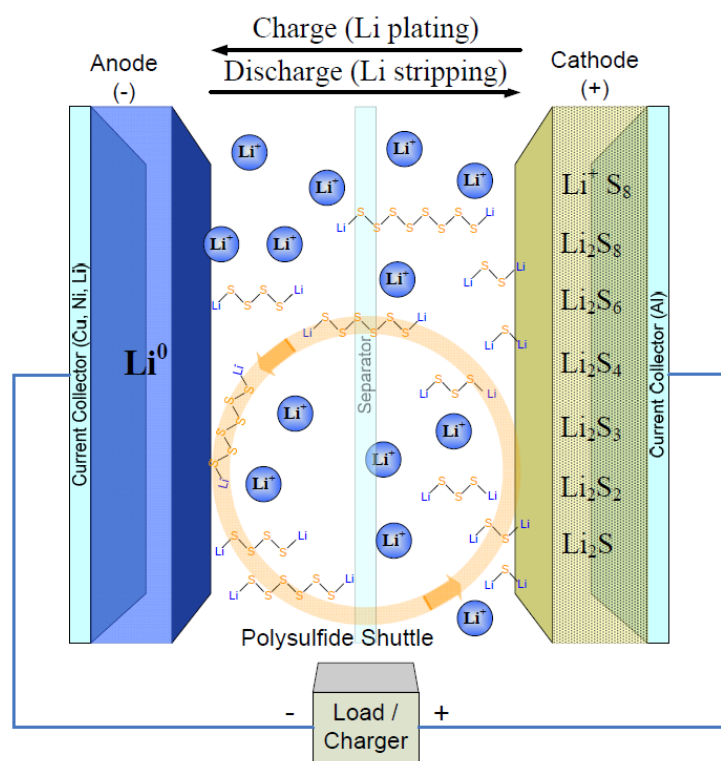


**Figure 4.** Traditional Li-S battery<sup>9</sup>

However, despite all their potential, lithium-sulfur systems suffer from a variety of currently uncured maladies. First, the lithium metal anode generates concern because of its reactivity. In scenarios involving cell damage or failings within the manufacturing process, fire or even explosion could result. Furthermore, lithium is susceptible to dendrite formation and “mossy” growth during cycling, potentially leading to cell failure and reduced energy density, respectively.<sup>10</sup> For the cathode, sulfur must be combined with conductive additives (usually carbon) because of its insulating nature, which in turn reduces the cell’s energy density.<sup>11-12</sup>

The stability of the electrolyte is also critical in response to the reactivity of the anode surface. Degradation of the electrolyte (both solvent and salt) occurs at the surface of the lithium metal, giving rise to the formation of a multicomponent film referred to as the solid-electrolyte interphase (SEI) layer. Its characteristics and nature are vital to the battery performance, as it is recognized as one of the many sources of irreversible capacity loss.<sup>13</sup> At the lithium anode, SEI properties are also expected to have a large impact in passivating the metal surface and controlling the formation of dendrites. However, the constituents of the SEI film, and by extension its properties as a whole, are almost entirely dependent upon the composition of the electrolyte. At the mesoscale, the formation of a solid electrolyte interphase on the surface of the electrode particles can also be disrupted due to cracking, causing it to spall off as a result of strains on the particles caused by lithium intercalation.<sup>5</sup> Not only does this lead to further fracture of the particles and eventual comminution, but the newly exposed surfaces cause even more SEIs to be formed, consuming lithium in a destructive side reaction which ultimately reduces the energy storage capacity of the cell.<sup>14</sup>

Perhaps the most difficult-to-overcome problem in lithium-sulfur batteries, however, is the transport (or shuttle) of lithiated, long-chain polysulfides migrating from the cathode to the anode.<sup>15-16</sup> These  $\text{Li}_2\text{S}_n$  ( $4 \leq n \leq 8$ ) species experience solubility within the electrolyte and are capable of diffusing to the anode and there undergoing additional reduction to ultimately produce insoluble  $\text{Li}_2\text{S}$  and  $\text{Li}_2\text{S}_2$ .<sup>11, 17</sup> This causes volume expansion of the anode crystal during their formation, and the subsequent SEI then passivates the lithium metal surface.<sup>13, 18</sup> Polysulfide shuttle is also capable of occurring



in the reverse direction, where the shorter chain, reduced, lithiated PS migrates back to the cathode, causing decreased coulombic efficiency and parasitic self-discharge.<sup>19-20</sup> In attempting to curtail these effects by keeping the PS away from the anode, a wide variety of unique architectures for cathode material have been tested, including carbon fibers, graphene, carbon nanotubes, and even conductive polymers.<sup>21</sup> Separators have also seen use in systems to minimize PS shuttle.<sup>22</sup>

At the other end of the research spectrum, first-principles calculations utilize the known quantum-mechanical interactions between atoms to predict the behavior of the macroscopic system. Since these calculations are only reliant on experimental data for validation, a wide variety of chemistries and conditions can be tested much more easily than by traditional methods.<sup>23</sup> This allows theory to complement experimental analysis by predicting the behavior of systems, their modes of failure, and their potential for improvement, all on the molecular level.<sup>24</sup> In the case of lithium-sulfur batteries, first-principles density functional theory (DFT) and ab initio molecular dynamics (AIMD) simulations can help identify the processes and mechanisms taking place within the cell and use this information to better understand and resolve some of these issues. Of particular interest is the effect of the lithium crystal structure, solvent, and salt used in a Li-S battery on the rate and pathway of the reactions occurring at the anode. The solvents considered in this thesis were 1, 2-Dimethoxyethane (DME) and 1, 3-Dioxolane (DOL), which see frequent use in lithium-sulfur systems, and ethylene carbonate (EC), a solvent common in traditional Li-ion batteries. 1,1,2,2-Tetrafluoroethyl 2,2,3,3-tetrafluoropropyl ether (D2) was also examined due to the interesting results obtained

by one of our collaborators when using it to replace DME in a binary solvent system.<sup>15</sup> Bis(trifluoromethane)sulfonimide lithium salt (LiTFSI) was chosen as a salt due to its excellent electrochemical properties and ubiquity in Li-S systems, and lithium bis(fluorosulfonyl)imide (LiFSI) was also studied due to its status as an up-and-coming additive capable of potentially replacing LiTFSI for Li-S applications.<sup>25</sup>

## Methodology

Using density functional theory, a body-centered cubic (BCC) lithium bulk crystal was optimized, with a calculated lattice parameter of 3.442 Å, which agrees well with experimental results.<sup>26</sup> Using this bulk crystal, two different crystallographic planes, (100) and (110), were constructed. These lithium crystal structures served as the representative electrode material for subsequent simulations involving the anode surface. The amount of volume made available for the electrolyte was roughly equal for both the (100) and (110) case (1613 and 1609 Å<sup>3</sup>, respectively). The three solvents mentioned earlier were also optimized using the Vienna *ab Initio* Simulation Package (VASP),<sup>27-28</sup> while the LiTFSI molecule was optimized using the Gaussian 09 (G09) package with a hybrid functional B3PW91 and the 6-311++G(p,d) basis set in order to determine the most favorable configuration of the lithium atom.<sup>29</sup>

The stability of solvent molecules near anode was studied using AIMD-based simulations which were performed upon the optimized representative lithium-metal surface which was in contact with the solvent in the liquid-phase within the NVT ensemble taken at 330 K and utilizing a 1-femtosecond time step. In order to achieve this time step, the mass of a proton is substituted for that of tritium. The Nose thermostat was

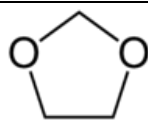
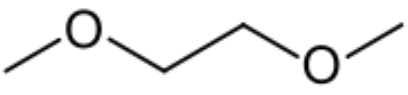
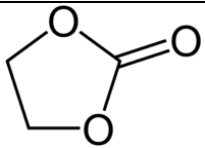
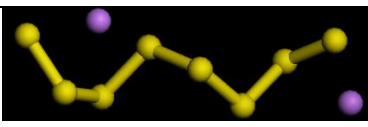
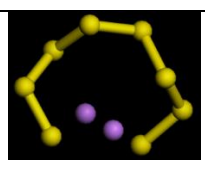
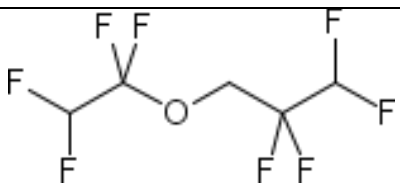
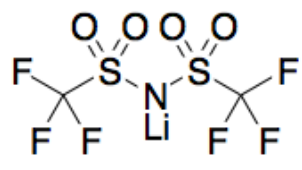
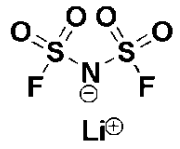
utilized to control temperature oscillations in the simulations using a Nose-mass parameter of 0.5, which yields an oscillation frequency corresponding to 176 time steps. The energy cutoff for the basis expansion of the plane-wave was taken to be 400 eV. Electron-ion interactions were represented using the pseudopotentials of the projector augmented wave (PAW), as given in the VASP databases.<sup>30</sup> The exchange-correlation functional was taken to be the Perdew-Burke-Ernzerhof generalized gradient approximation (GGA-PBE), and a conjugate-gradient algorithm was also utilized to achieve relaxation of the ions into their instantaneous ground state.<sup>31</sup> Also, a Gaussian smearing with a 0.05 eV width was used, and for the Brillouin zone integration of the surface, the Monkhorst-Pack k-point mesh was taken to be  $4 \times 4 \times 1$ . Convergence criteria for ionic relaxation and electronic self-consistent iteration were set to  $10^{-3}$  and  $10^{-4}$  eV, respectively.

Both pure solvents and mixtures were investigated, although the main focus of this thesis will be on the binary mixture results. The density of liquid-phase solvents was approximated by randomly placing 9, 13, and 14 molecules of DME (density = 0.87 g/cm<sup>3</sup>), DOL (density = 1.06 g/cm<sup>3</sup>), and EC (density = 1.32 g/cm<sup>3</sup>) in contact with the lithium metal surface, respectively. Next, the liquid-phase solvent molecules were permitted to relax through the use of a classical molecular mechanics minimization. In this minimization, the consistent valence force field (CVFF) using a conjugate gradient algorithm within the Materials Studio software was employed. The maximum cumulative force of the system atoms necessary for convergence was taken to be 0.005 kcal mol<sup>-1</sup> Å<sup>-1</sup>.

Afterward, the minimized solvent-anode systems were allowed to run for up to 20 ps of AIMD simulation. A similar procedure was employed with binary solvent mixtures, where the mixture concentration was taken to be 1:1 v/v, following literature reports.<sup>11</sup> In subsequent simulations, the salt decomposition and its effect on the model lithium-metal anode surface was evaluated by adding 1-4 M of the LiTFSI or LiFSI salt to the pure or binary solvent system in contact with the model Li surface. Given the volume of the simulation cell, only one salt molecule was required to reach a 1 M concentration. Later, lithiated PS molecules ( $\text{Li}_2\text{S}_8$ ) in both linear and ring configurations were also added to the model electrolyte, with concentrations ranging from 1-3M. These were optimized through the use of the G09 package software, performed at an identical level of aforementioned theory.

In addition, the energy of a neutral  $\text{Li}_2\text{S}_8$  molecule was first calculated, and subsequently, fragments and potential decomposition products were optimized to evaluate the most thermodynamically favorable reduction pathways.  $\text{Li}_2\text{S}_8$  molecules were then added to the mixtures of solvents and salt, and the effects of the PS on the electrolyte and its decomposition on the lithium-metal anode were investigated using AIMD simulations at 330 K with the same simulation parameters reported previously. The properties of the electrolyte components are given in Table 1 below.

**Table 1.** List of electrolyte component properties

Species Name	Mol. Wt.	Density	Structure
Dioxolane (DOL)	74.08 g/mol	1.06 g/cm <sup>3</sup> 32	
Dimethoxyethane (DME)	90.12 g/mol	0.87 g/cm <sup>3</sup> 33	
Ethylene Carbonate (EC)	88.06 g/mol	1.32 g/cm <sup>3</sup> 34	
Li <sub>2</sub> S <sub>8</sub> (Linear)	269.88 g/mol	Varies	
Li <sub>2</sub> S <sub>8</sub> (Ring)	269.88 g/mol	Varies	
1,1,2,2-Tetrafluoroethyl 2,2,3,3-tetrafluoropropyl ether (D2)	232.07 g/mol	1.53 g/cm <sup>3</sup> 35	
Bis(trifluoromethane) sulfonimide lithium salt (LiTFSI)	287.09 g/mol	Varies	
Lithium bis(fluoro- sulfonyl) imide(LiFSI)	187.08 g/mol	Varies	

A representative system of a DOL/DME mixture containing 1 M LiTFSI is shown in Figure 5 below at 0 ps of simulation time.

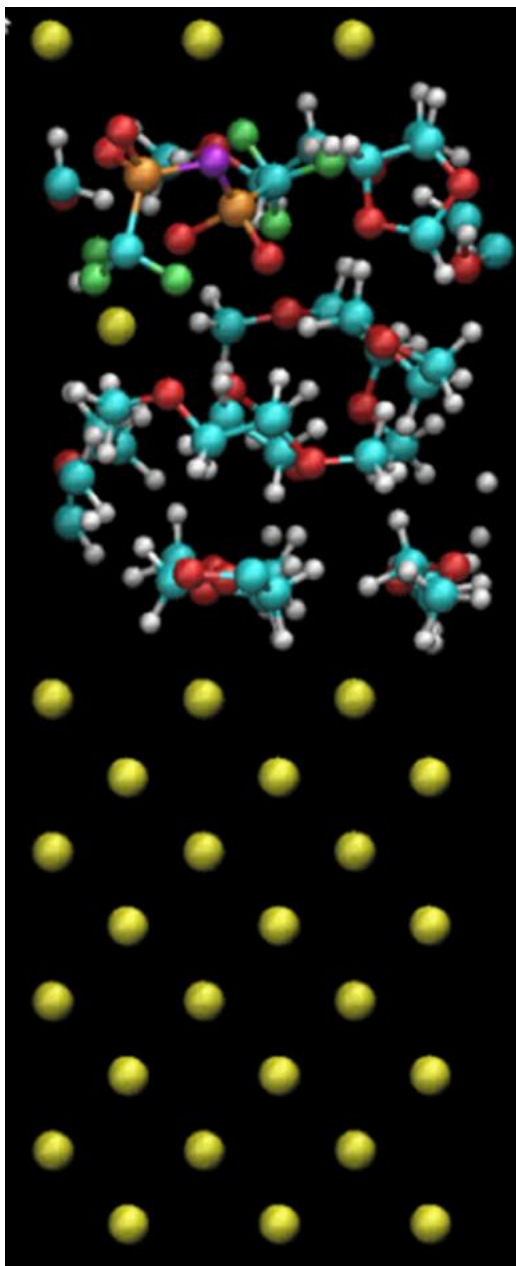


**Figure 5.** DOL/DME, 1 M LiTFSI system. Color key: red, oxygen; white, hydrogen; blue, carbon; yellow, lithium; orange, sulfur; purple, nitrogen; green, fluorine.

## CHAPTER II

### EFFECTS OF LITHIUM SURFACE STRUCTURE

Electrolyte stability is critical to the performance and cyclability of the lithium-sulfur battery, as any side reactions of the solvent and/or salt tend to decrease the energy density of the system due to the need for excess electrolyte to account for the degradation. Furthermore, the products of such reactions often migrate to the lithium surface where they either diffuse into the bulk, disrupting the microstructure, or stay at the surface, forming an SEI which typically hampers lithium transport. Not only can the SEI lead to longer charge/discharge times, but it also consumes lithium in the process, again reducing the battery's energy density.

One of the challenges in creating a suitable electrolyte, however, is the lack of a “perfect” solvent, one with ideal properties for Li-S applications. For instance, the most stable solvent molecules are shorter linear ethers or cyclic ethers, as these are more stable than aromatic ones with conjugated rings.<sup>36</sup> The ideal solvent for lithium-sulfur batteries will have uniform charge distribution, a shorter chain length, and non-conjugated rings. Furthermore, solvent viscosity can have a dramatic impact on lithium ion movement through the electrolyte as well as affecting dendritic growth. High interfacial energy between the solvent and lithium surface can also retard dendrite formation, so solvents with methyl groups are preferable. The challenge is that high ionic conductivity solvents tend to also have high viscosities, and vice-versa, meaning that no single solvent possesses all the desired electrolytic properties.

For these and other factors, solvent mixtures have been proposed as a viable way to optimize electrolyte properties by combining the positive aspects of various compounds. In this thesis, binary mixtures of some common solvents were simulated with AIMD to determine their behavior at the lithium metal surface. Initially, no salt molecules were added in order to isolate solvent behavior. In choosing solvent mixtures for Li-S systems, the most obvious choice was a mixture of DOL/DME, which is a relatively common combination used in Li-S batteries and has shown promising results, often in a 1:1 volume ratio.<sup>11</sup> In addition to using a 1:1 v/v mixture of DOL/DME, EC was also considered due to its ubiquity in traditional Li-ion cells. Since EC possesses some very desirable properties, it was important to determine if this more reactive molecule could be stabilized through the addition of other, more stable solvents, in this case DOL and DME. The procedure mentioned in the introduction was used to fill the volume of the crystal vacuum slab; to wit, the densities of the solvent and the volume of the slab were used to determine the number of molecules of each solvent needed to achieve equal volumes.

The first solvent mixture under consideration is EC/DME. Based on the densities of these compounds (given in the Introduction), seven molecules of EC and five molecules of DME were placed within the crystal vacuum slab in Materials Studio and then made to undergo a geometry optimization using Forcite analysis. In the case of the (100) crystal, the middle three layers are fixed to expedite the AIMD simulation, while in the (110) lattice the middle two were fixed. Figure 6 below shows the EC/DME solvent mix with the (100) crystallographic plane.



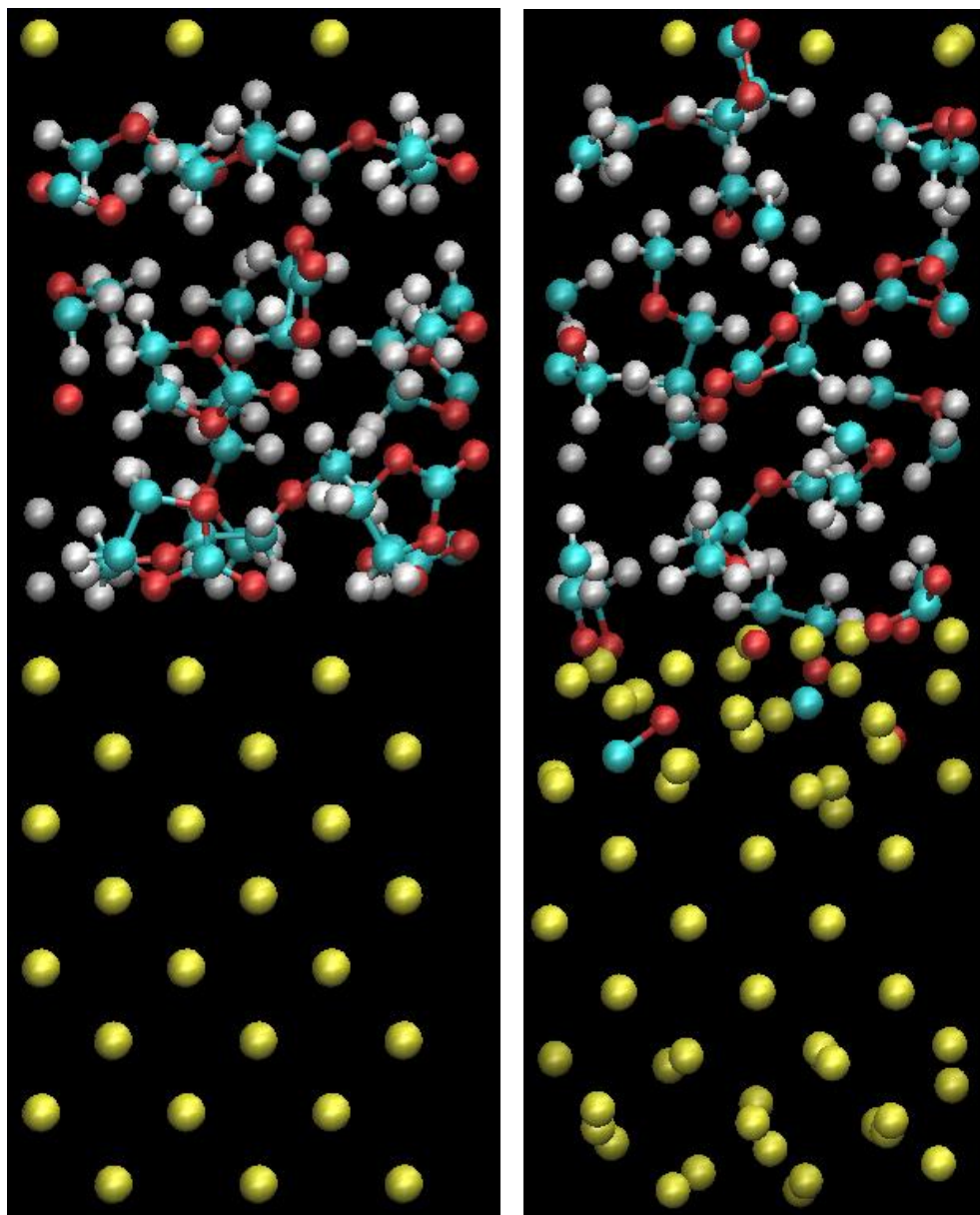


**Figure 6.** Left: EC/DME, (100) at 0 ps. Right: at 15.8 ps. Color key: red, oxygen; white, hydrogen; blue, carbon; yellow, lithium

Here the EC exhibits high reactivity at the anode, as only three of the initial seven molecules avoid decomposition. For the DME, all five are intact after 15.8 ps. For

comparison, the (110) lithium case with seven molecules of EC and five molecules of DME is shown below in Figure 7.

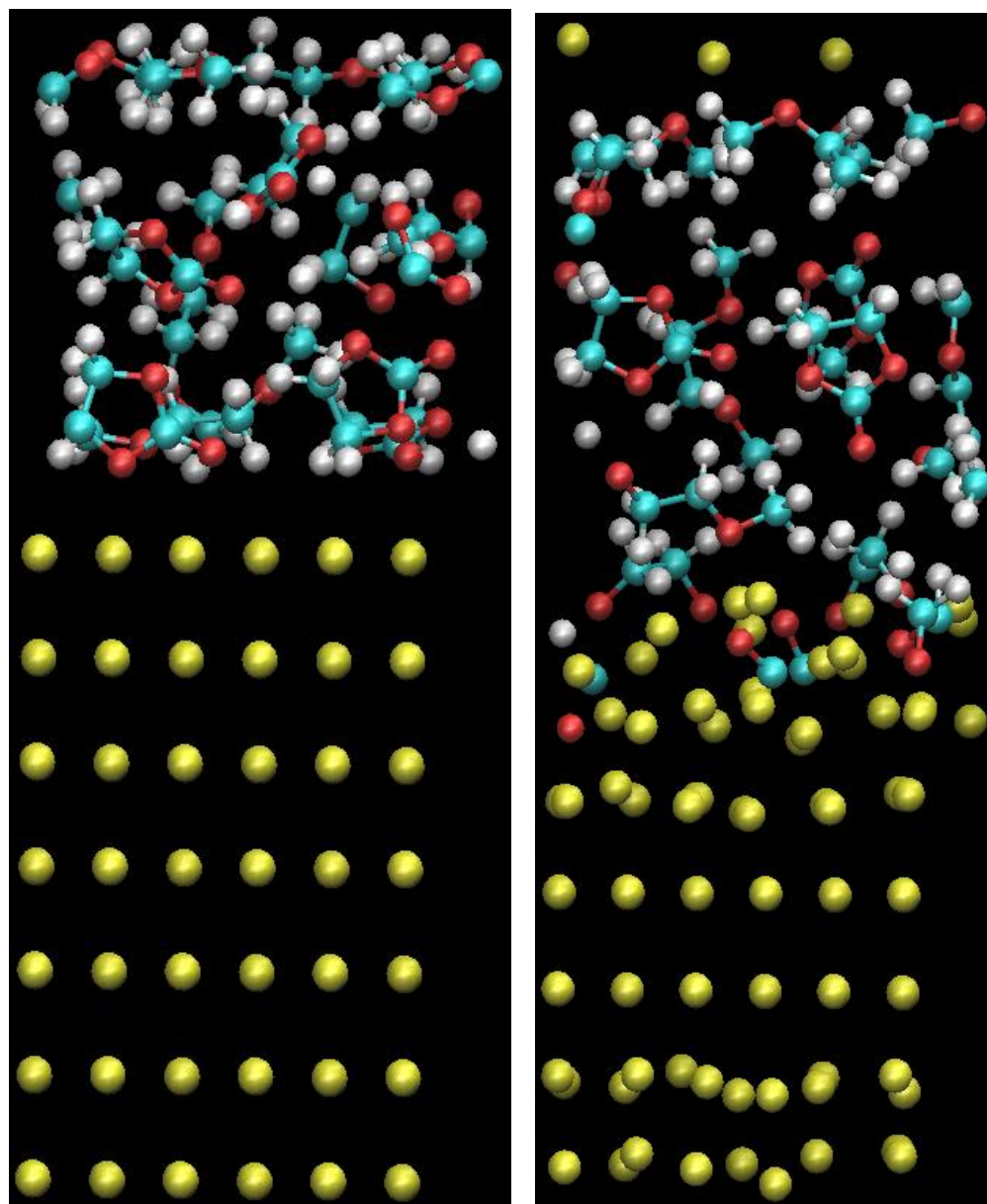


**Figure 7.** Left: EC/DME, (110) at 0 ps. Right: at 14.6 ps. Color key: red, oxygen; white, hydrogen; blue, carbon; yellow, lithium

For this system, four out of seven EC molecules avoided decomposition, while all five DME molecules remained intact. All three EC reactions produced CO and C<sub>2</sub>H<sub>2</sub>O<sub>2</sub>.

The second solvent mixture, EC/DOL, consisted of seven molecules of EC and six of DOL based on the solvent densities. The results for the (100) lithium crystal are shown in Figure 8 below.

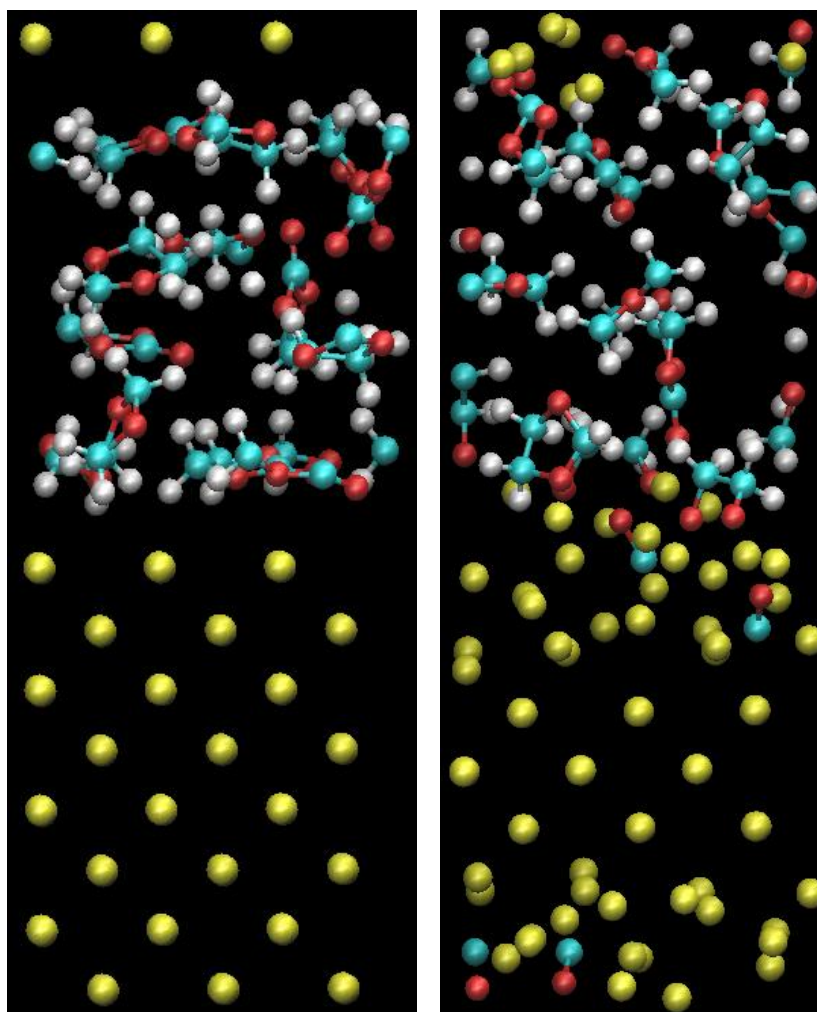


**Figure 8.** Left: EC/DOL, (100) at 0 ps. Right: at 16.6 ps. Color key: red, oxygen; white, hydrogen; blue, carbon; yellow, lithium

In this case, the EC solvent also undergoes significant decomposition, with five of the seven initial molecules decomposing within 16.6 ps. The decomposed EC tends to either form CO (three occurrences) or C<sub>2</sub>H<sub>2</sub>O<sub>2</sub> (four occurrences). DOL, on the other hand, remains quite stable, with all six molecules surviving for the duration of the simulation.

For the (110) EC/DOL mixture, the results are seen in Figure 9 below. We can see that after 16.1 ps, only three of the initial seven EC molecules survive without decomposition, while all six DOL molecules do. Also, all four EC decomposition reactions produce CO and C<sub>2</sub>H<sub>2</sub>O<sub>2</sub>, as seen in the EC/DME case.

Finally, DOL/DME was considered, with six molecules of DOL and five of DME yielding a 1/1 v/v ratio. The results of the (100) crystal simulation are seen in Figure 10 below. From these results, we see that for both solvents no decomposition is seen within the simulated timeframe. The (110) crystal case is shown in Figure 11 below.

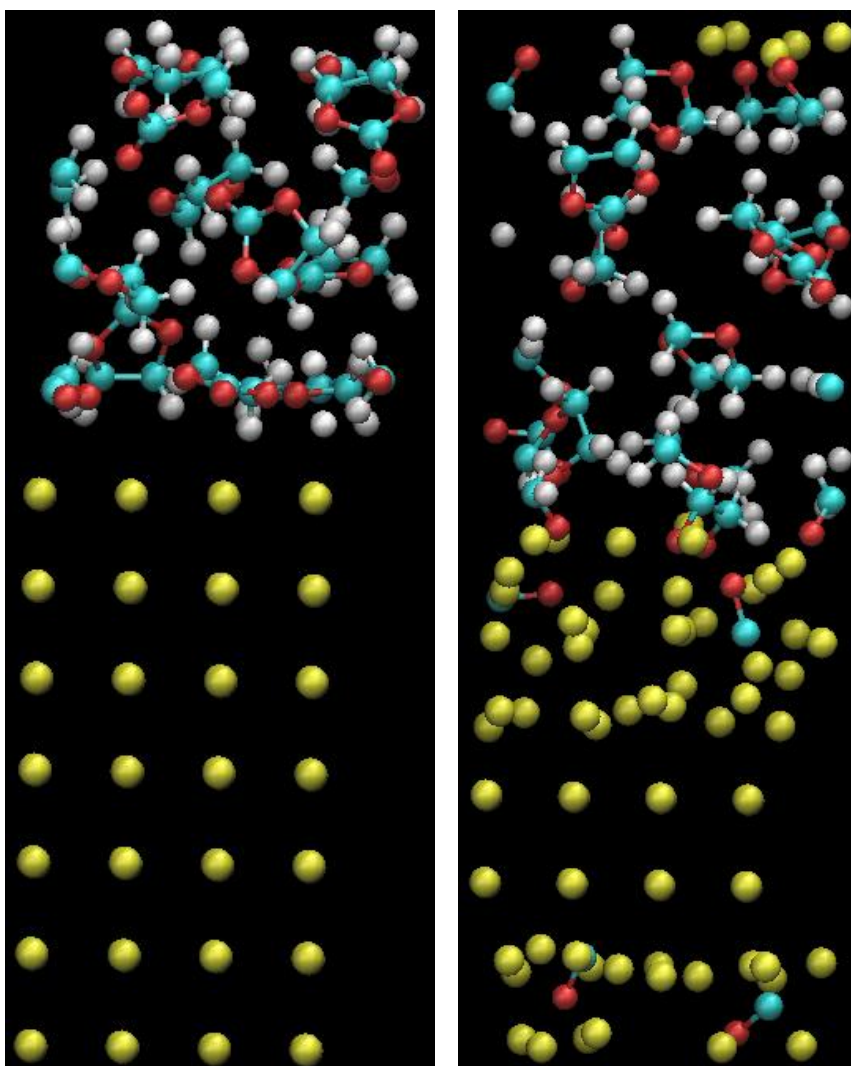


**Figure 9.** Left: EC/DOL, (110) at 0 ps. Right: at 16.1 ps. Color key: red, oxygen; white, hydrogen; blue, carbon; yellow, lithium

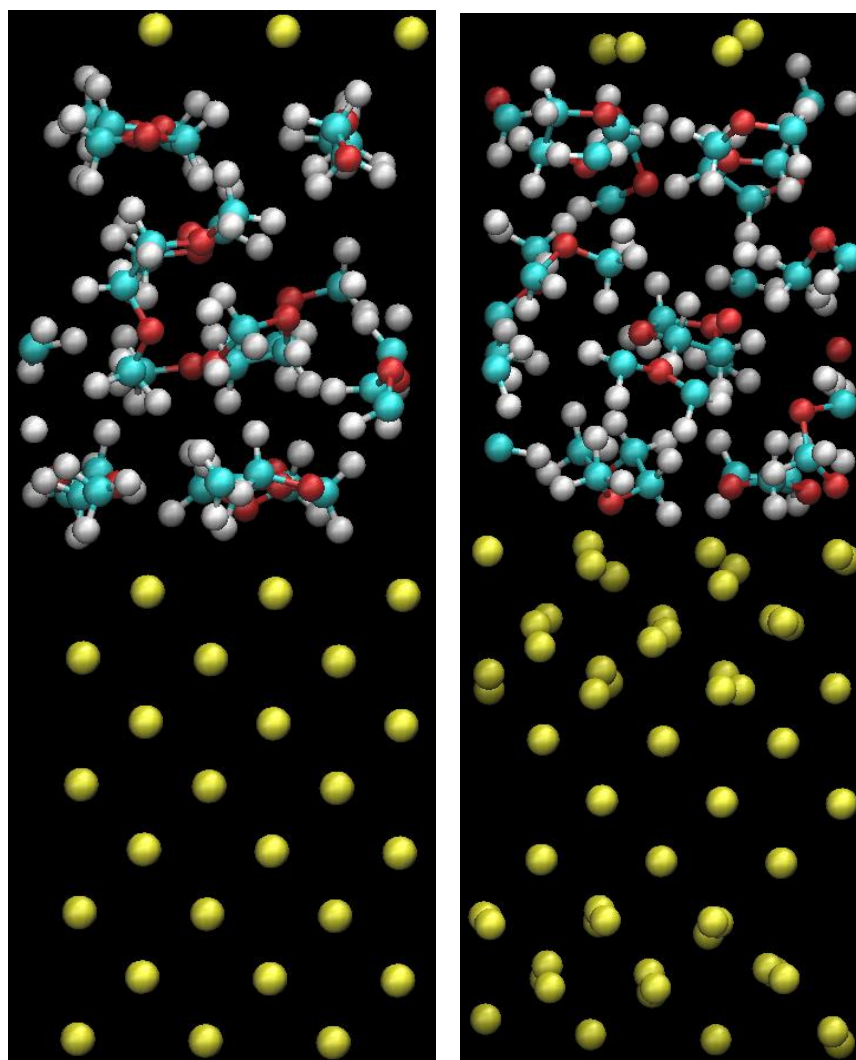


**Figure 10.** Left: DOL/DME, (100) at 0 ps. Right: at 17.4 ps. Color key: red, oxygen; white, hydrogen; blue, carbon; yellow, lithium

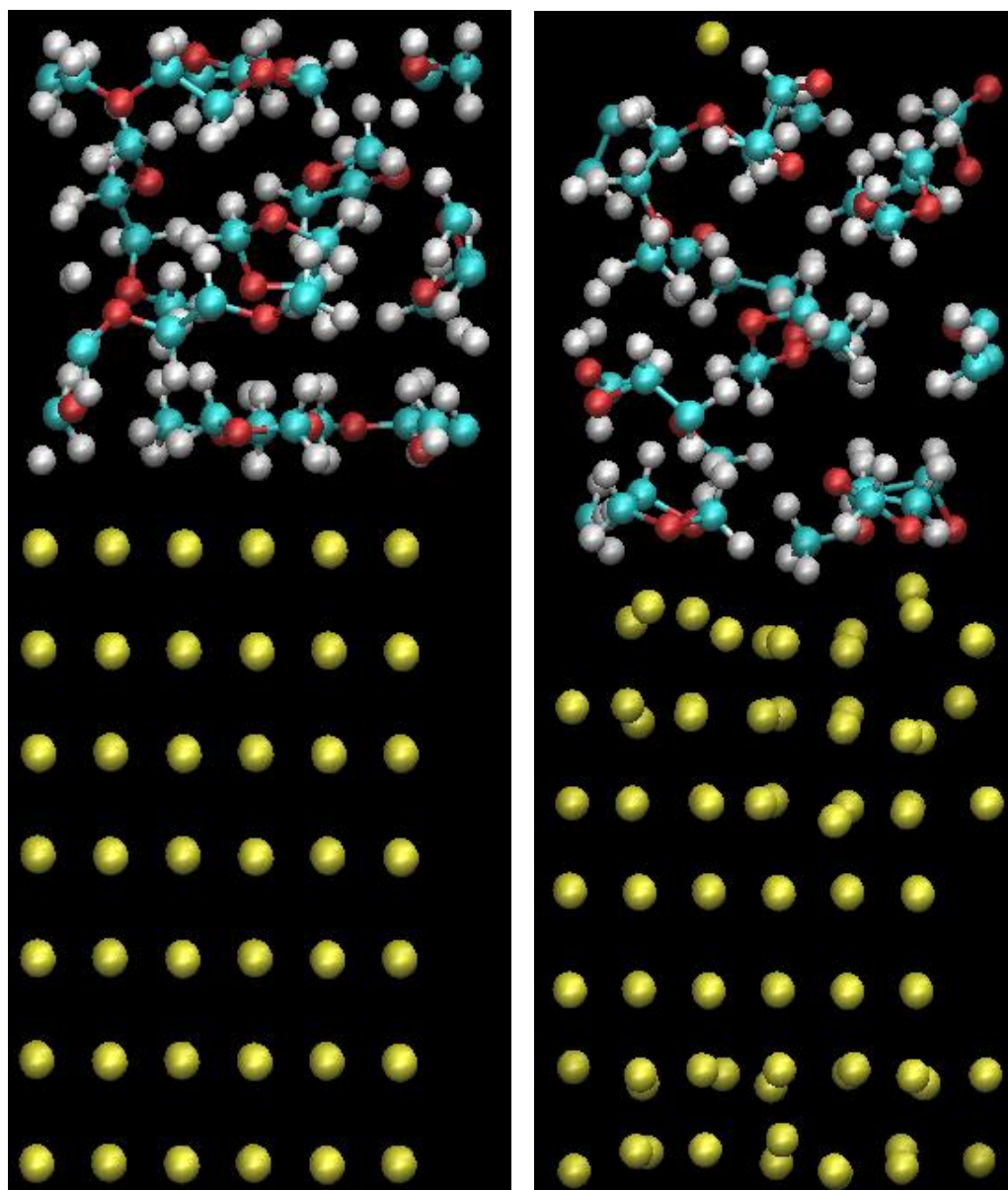


**Figure 11.** Left: DOL/DME, (110) at 0 ps. Right: at 16.7 ps. Color key: red, oxygen; white, hydrogen; blue, carbon; yellow, lithium

Again, no solvent reduction is seen in this simulation. Figure 12 summarizes the results of the AIMD simulations thus far.

## EC-DME

Crystal	Time	EC initial	EC final	DME initial	DME final
Li (100)	15.8 ps	7	3	5	5
Li (110)	14.6 ps	7	4	5	5

## EC-DOL

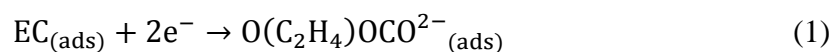
Crystal	Time	EC initial	EC final	DOL initial	DOL final
Li (100)	16.6 ps	7	2	6	6
Li (110)	16.1 ps	7	3	6	6

## DOL-DME

Crystal	Time	DOL initial	DOL final	DME initial	DME final
Li (100)	17.4 ps	6	6	5	5
Li (110)	16.7 ps	6	6	5	5

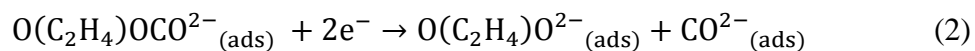
**Figure 12.** Summary of solvent reactivity results for (100) and (110) crystals

From this, we can gather a few important conclusions about solvent reactivity and the impact of the lithium crystal structure. First, EC is very reactive at the anode surface, regardless of the crystal structure used. It almost always reduces via the following two sequential reactions. Reaction 1 involves the opening of the EC ring via the cleaving of either of the oxygen and ester-carbon single bonds.



Once the ring has been opened, the previously double-bonded oxygen and carbon atoms break from the remainder of the molecule by Reaction 2.





These final products have been observed in each case of EC decomposition occurring in the systems thus far considered, and are stable enough to survive at the lithium surface for almost 20 ps of simulations time. Secondly, both the DOL and DME show great stability at the anode, both in the bulk solvent and just a few angstroms from the metal surface. Because of this stability, or rather the comparative instability of EC in this environment, subsequent electrolyte simulations will mostly use DOL, DME, or mixtures of the two.

Finally, we come to the issue of the lithium crystal structure and its impacts. From a comparison of the (100) and (110) structures at the beginnings and ends of their respective simulations, it is evident that the crystal structures evolve with time. The (100) tends to expand from its initial configuration, even when diffusion of EC decomposition products into the bulk is not a factor, as in the DOL/DME case. In contrast, the (110) crystal seems to contract, even when decomposition products are present. This may be due to instability of the lithium crystal in this environment, leading to a collapse from the initial lattice structure. From Figure 13, it appears that the (100) crystal structure may be slightly less favorable for use with EC than the (110), but for this small number of molecules and smallest of differences such a conclusion is difficult to confirm, especially since the (110) crystal systems ran for a slightly shorter simulation time. These results may also be due to the lithium expansion/contraction behaviors noted above, as a smaller volume for the vacuum slab (resulting in a higher solvent concentration) drives solvent diffusion into the bulk, often leading to increased

reactivity. What we can say with certainty is that for both crystal structures, DOL and DME are very stable at the anode surface, even when other electrolyte components degrade. For this reason, the desire to limit calculations, the apparent instability of the (110) crystal, and for the sake of consistency with the simulations performed by my fellow researchers, the (100) structure was chosen for use in the remainder of the simulations performed in this thesis.

## CHAPTER III

### EFFECTS OF ELECTROLYTE COMPOSITION

#### **Salt**

In addition to the solvent effects and behavior described in the previous chapter, a traditional battery electrolyte is also comprised of lithium salts. In a traditional Li-ion battery, salts like  $\text{LiPF}_6$  and  $\text{LiClO}_4$  are common and added to an organic solvent to form a liquid electrolyte, whose purpose is to allow cation transfer upon discharge. Common solvents are carbonates such as ethylene carbonate or diethyl carbonate, and a combination of both cyclic and linear species is beneficial to the electrolyte conductivity. However, as has been shown in the previous chapter, carbonates are quite unstable at the anode, and for this reason (and others), EC is not commonly used in Li-S systems.

But what if an additive could further improve the performance of the solvent mixture? This brings us to the same setup as seen in traditional Li-ion cells, namely that by adding a salt (such as  $\text{LiPF}_6$ ,  $\text{LiNO}_3$ , or  $\text{LiTFSI}$ ) we can improve the electrolyte conductivity, stability at the anode, resistance to dendritic growth, etc. In some cases, the salt can actually lead to the formation of a beneficial SEI, as was seen with  $\text{LiPF}_6$ , which helped to make rechargeable LIBs economically viable.<sup>37</sup> An important lesson can be learned from this specific salt: all of its desirable properties are surpassed in other salts, yet the combination of them in  $\text{LiPF}_6$  is ideal for the rechargeable LIB application.

In the case of lithium sulfur batteries, the same idea applies. All salt candidates must juggle many diverse and sometimes contradictory properties themselves, in addition to supplementing specific solvent properties. In this thesis, two different salts

were examined: LiTFSI and LiFSI, both of which promise to help resolve the electrolyte limitations encountered thus far in Li-S cells. LiTFSI has become a rather common solvent in these applications,<sup>38-39</sup> while LiFSI is less commonly encountered.<sup>25</sup> Both salts were tested with the same mixtures of electrolytes as described in chapter one, i.e., 1:1 v/v mixtures of EC/DME, EC/DOL, and DOL/DME. Salt concentration was taken to be 1M, which corresponded to one salt molecule for the simulated volume. Since lithium crystal structure does not appear to impact the solvent stability, as seen in Chapter II, for simplicity's sake all AIMD electrolyte simulations were conducted with the (100) crystal structure.

In the case of EC/DME, the initial configuration of the system is shown below in Figure 13, alongside the configuration after 8.7 ps of AIMD simulation. It should be noted that the desired simulation time was around 8 ps, and that there will be minor fluctuations in the simulation time between different systems based upon the number of atoms the system contains.

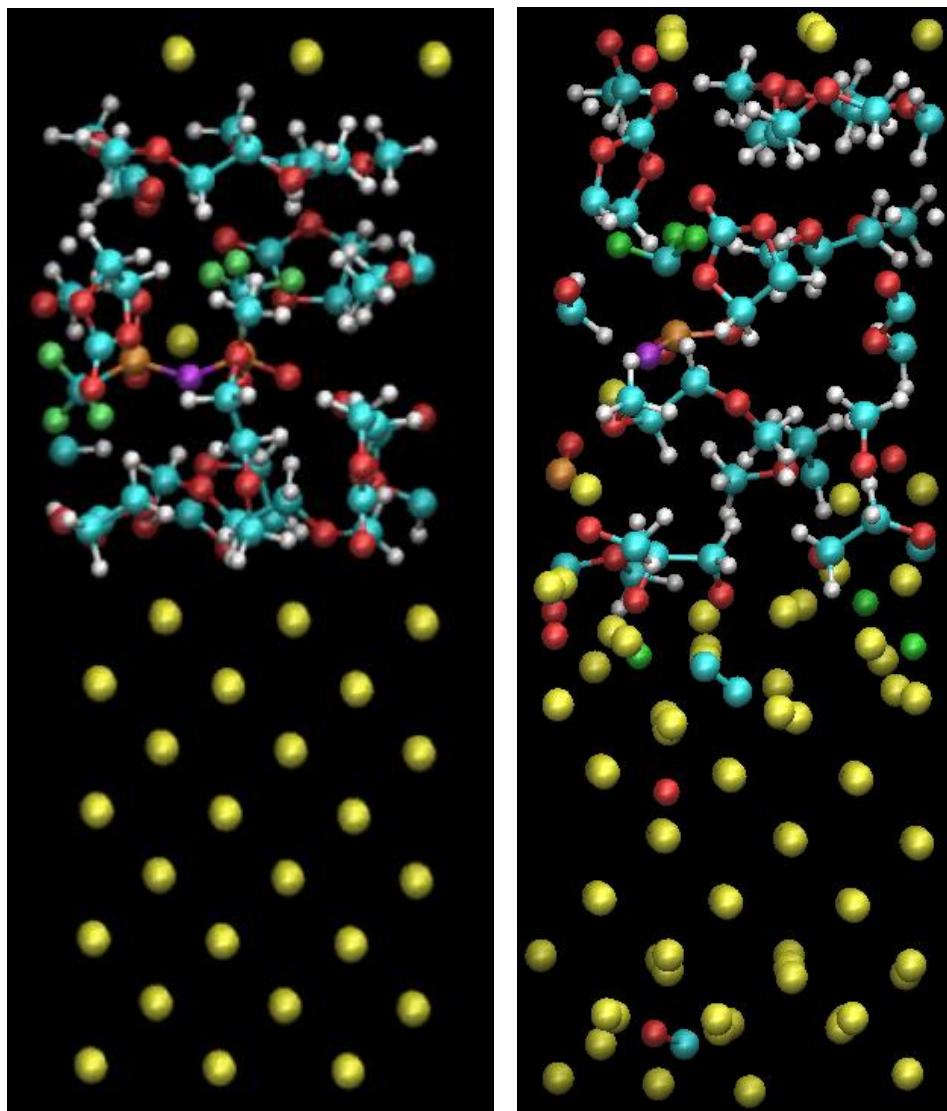


**Figure 13.** Left: EC/DME, 1M LiTFSI at 0ps. Right: EC/DME, 1M LiTFSI at 8.7 ps. Color key: red, oxygen; white, hydrogen; blue, carbon; yellow, lithium; orange, sulfur; purple, nitrogen; green, fluorine.

As can be easily gathered from the images above, several reactions occurred over the course of the simulation. This seems to support our previous observations concerning EC reactivity. In total, even with the addition of LiTFSI, four of the seven EC molecules decomposed, while all five DME molecules remain intact. These are exactly the same

results seen without the addition of the salt. The first EC reaction occurs at 0.45 ps, while the last happens at 6.24 ps. Only the molecules near the lithium surface reacted; the EC in the bulk of the electrolyte does not decompose over this time frame. After reacting, the EC fragments at the Li surface begin to diffuse into the bulk anode material, some quite a distance. One oxygen atom from an EC decomposition has migrated more than 5 Angstroms into the metal bulk and is only stopped by the fixed layers of lithium atoms.

Meanwhile, the salt itself does not fare well in this simulation. Within 0.2 ps the backbone breaks via an S-N bond. The resulting  $\text{SO}_2\text{CF}_3$  fragment then slowly migrates to the lithium surface, while the other half of the LiTFSI molecule remains in the bulk. After 5 ps, the  $\text{CF}_3$  group breaks from the  $\text{SO}_2$  and subsequently approaches the anode, as shown in Figure 14.

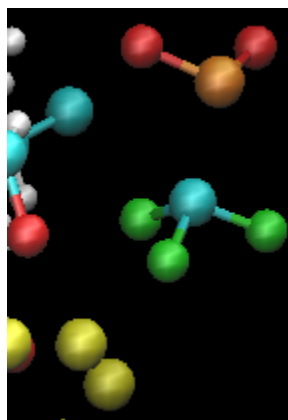


**Figure 14.**  $\text{CF}_3$  group leaving

At 5.3 ps, the fluorinated methyl group begins to defluorinate, with the fluorine atom then diffusing into the bulk metal. After losing a second fluorine, the carbon then reattaches to the SO<sub>2</sub> group. By 5.8 ps, the carbon is completely defluorinated. It then interacts with other EC decomposition products to produce a metastable ether. In contrast, the other half of the LiTFSI molecule remains unreacted in the bulk, although there seems to be a strong interaction with the rest of the severed molecule. This is seen in Figure 15. The lithium atom from the salt seems to form a bridge between the two LiTFSI fragments.



**Figure 15.** Salt at the end of EC/DME simulation

As for the simulation decomposition products, atomic fluorine from the salt is found at the lithium surface, while atomic oxygen seems to more readily diffuse into the bulk. Diatomic carbon can also be seen, as well as carbon monoxide. The most prevalent

species, however, is the EC decomposition product  $C_2O_2H_4$ , with three occurrences being found in this simulation, just as we saw in the previous chapter. One such molecule is shown below at the end of the simulation in Figure 16. In the three occurrences of this species, all are oriented with the oxygen atoms facing the positively charged lithium surface, stabilized by the presence of the lithium atoms.

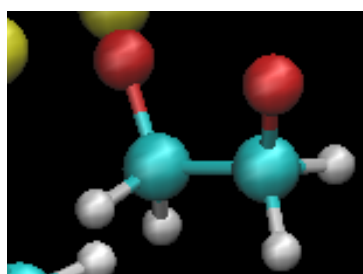


**Figure 16.**  $C_2O_2H_4$  near the lithium surface

For the case of EC/DOL, the initial and final configurations are shown below in Figure 17.



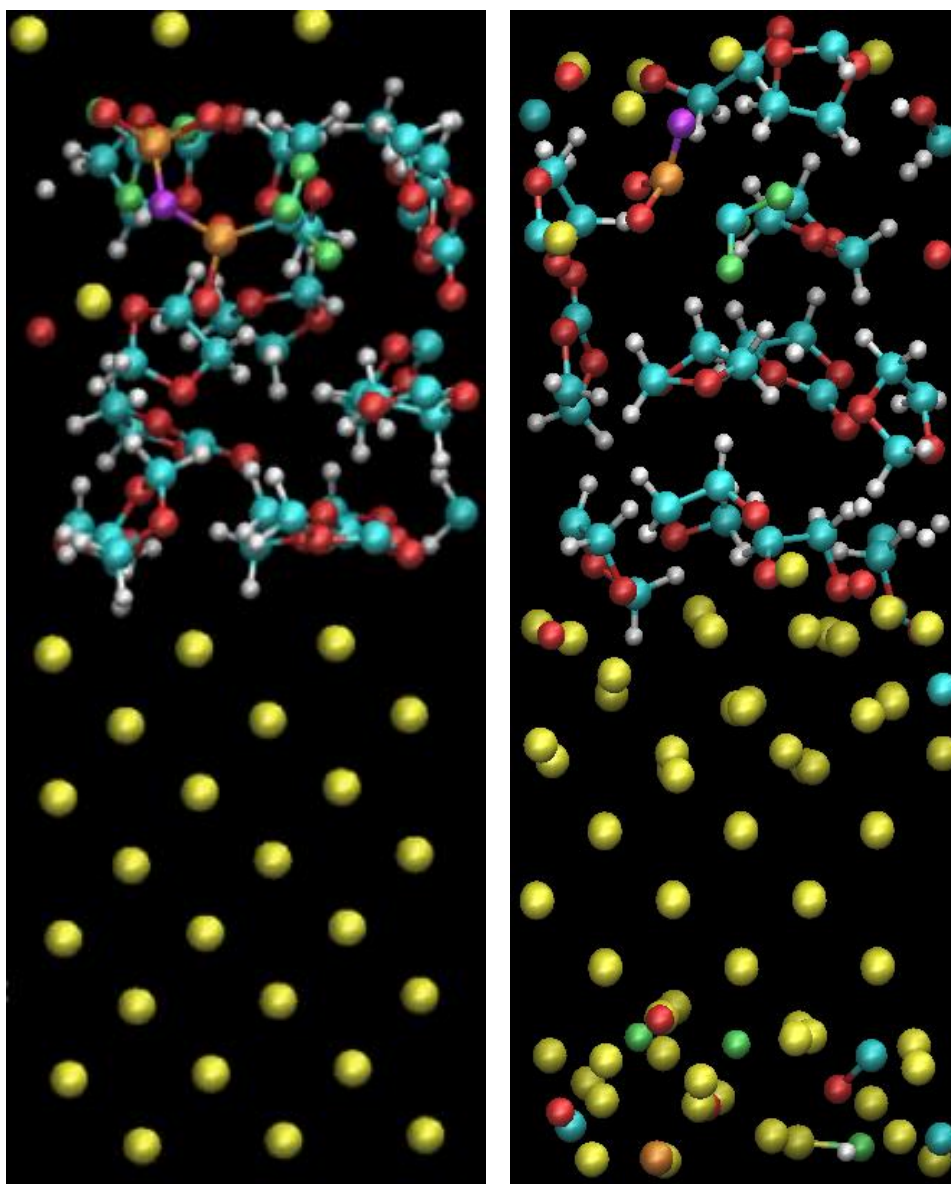


**Figure 17.** Left: EC/DOL, 1M LiTFSI at 0ps. Right: EC/DOL, 1M LiTFSI after 7.8 ps. Color key: red, oxygen; white, hydrogen; blue, carbon; yellow, lithium; orange, sulfur; purple, nitrogen; green, fluorine.

Again, with EC present several reactions take place. After 7.8 ps, four out of the seven initial EC molecules have decomposed, with all of the DOL molecules surviving until the end of the simulation. The first EC ring opens at 0.54 ps, while the last occurs at

3.7 ps. In this system, the LiTFSI salt was placed closer to the lithium surface, with one F atom within 2 Å of the crystal lattice. Consequently, we see the salt begin to decompose very rapidly (within 0.1 ps) via the breaking of C-F and C-S bonds, which occur roughly simultaneously. The resulting CF<sub>2</sub> group then rapidly migrates to the lithium surface, and by 0.4 ps the carbon has been completely defluorinated.

The remainder of the salt then also migrates to the anode surface, as shown in Figure 18.



**Figure 18.** Salt configuration in EC/DOL at 1 ps.

The salt fragment, while relatively stable in the bulk electrolyte, undergoes reactions at the metal surface, starting with the fracture of the upper N-S bond at 1.5 ps. This results in an SO<sub>2</sub> group that stays at the surface as shown in Figure 19, and survives until the 5.2 ps mark, when one O-S bond is broken.

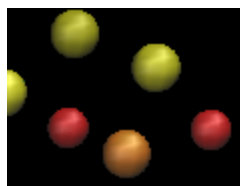


**Figure 19.** SO<sub>2</sub> group at the anode surface at 5.2 ps.

By 5.6 ps the second oxygen atom leaves, and the lone S atom goes on to interact with lithium atoms, which in turn seem to be interacting with the nitrogen of the main LiTFSI fragment as seen in Figure 20.



**Figure 20.** Lithium, nitrogen, sulfur interaction at the anode surface.

This behavior is intriguing because we see what appears to be the formation of a Li<sub>2</sub>S molecule, albeit one seemingly stabilized by the nucleophilic nitrogen of the salt. The formation of this species is very commonly reported in Li-S systems, and is one of the primary causes of irreversible capacity loss. The fact that we observe the same behavior, even with only one free sulfur atom in the system indicates the favorability of this reaction pathway. Meanwhile, the remainder of the salt molecule survives until the end of the simulation time.

For the final case of DOL/DME, we expect to see a much less reactive solvent mixture due to the absence of EC. From the previous two AIMD simulations, neither DME nor DOL have reacted, and this trend continues here, as shown in Figure 21 below.

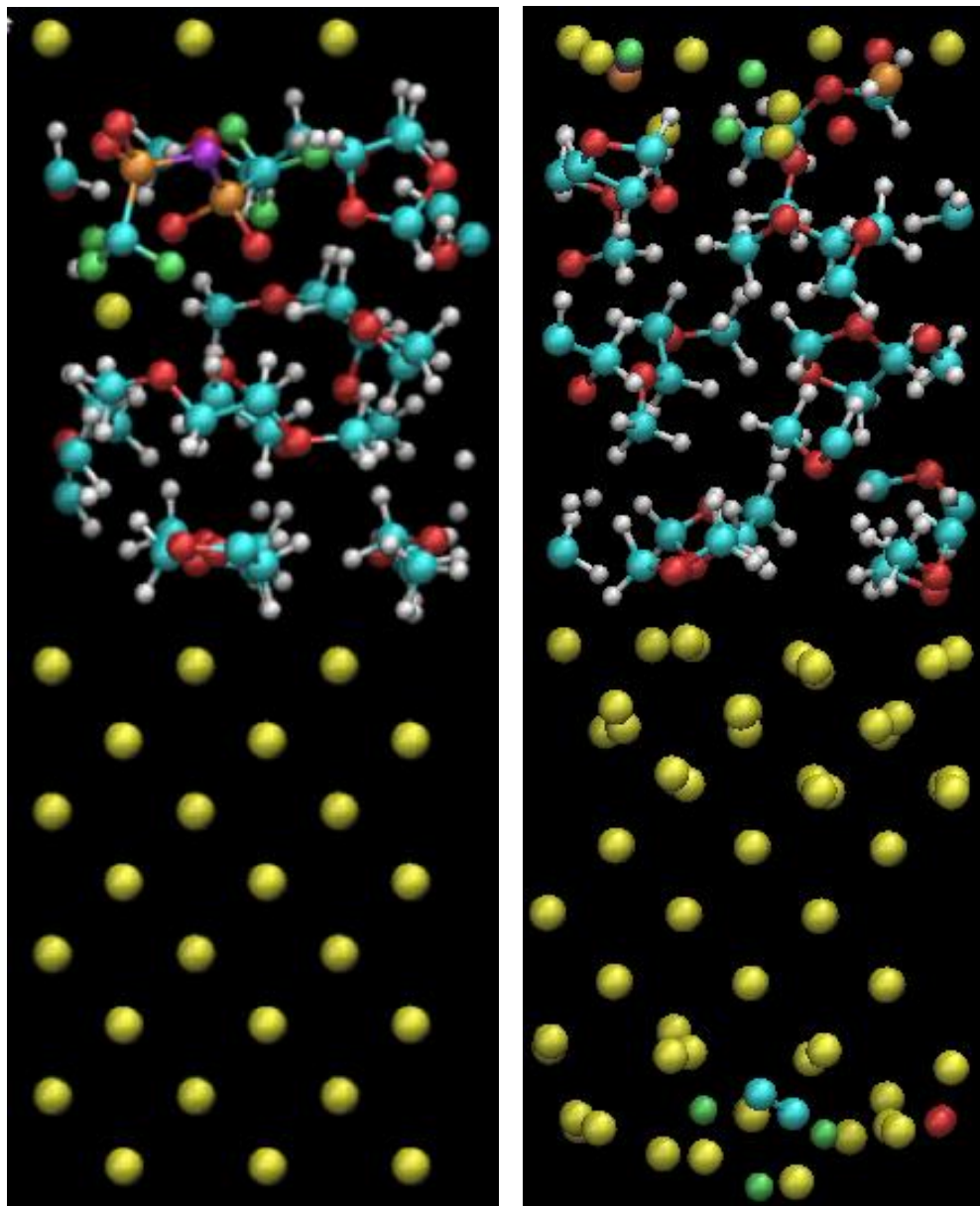


**Figure 21.** Left: DOL/DME, 1M LiTFSI at 0ps. Right: DOL/DME, 1M LiTFSI after 9.2 ps. Color key: red, oxygen; white, hydrogen; blue, carbon; yellow, lithium; orange, sulfur; purple, nitrogen; green, fluorine

Compared to the runs using EC, this system is inert over this timeframe, save for the reactions of the salt. This time, the salt decomposes via an N-S bond within 0.1 ps, with the nitrogen-containing fragment then migrating to the anode surface, where it undergoes further decomposition. Both  $\text{CF}_3$  groups are completely defluorinated, and by the end of the simulation the only fragments left intact are an  $\text{SO}_2$  group and an S-N linkage from the original salt backbone.

To summarize these results, we can see that while EC may have some beneficial properties for the electrolyte, its reactivity near the lithium surface makes it unsuited for Li-S applications, and even with the LiTFSI salt helping to passivate the anode surface, EC stability in this environment is not ameliorated. In contrast, both DOL and DME seem to show high stability, even at the anode surface, making them both strong candidates for Li-S systems. These first-principles results seem to support the experimental findings for different solvent systems and mixtures and help provide a rationale for the excellent performance seen in some DOL/DME solvent systems. It is important to note that the DOL/DME will eventually decompose at the anode, just at a much longer time scale than what was used in these simulations.

### **Polysulfides**

As we noted in the Introduction, the decomposition process of the long-chain PS molecules occurring during the battery discharge is one of the most challenging features of the lithium-sulfur battery system to adequately understand and therefore engineer.<sup>40</sup> At the start, long-chain sulfur species from the cathode ( $\text{S}_8$ ) react with the lithium ions dissolved in the electrolyte to produce  $\text{Li}_2\text{S}_8$ .<sup>41</sup> Even after successive charge and

discharge cycles, this species is normally not oxidized back to its elemental components.<sup>42</sup> The standard mechanism for reaction of the lithiated polysulfide upon discharge is taken to be:  $\text{Li}_2\text{S}_8 \rightarrow \text{Li}_2\text{S}_6 \rightarrow \text{Li}_2\text{S}_4 \rightarrow \text{Li}_2\text{S}_2 \rightarrow \text{Li}_2\text{S}$ .<sup>10</sup>  $\text{Li}_2\text{S}_2$  and  $\text{Li}_2\text{S}$  are particularly important because both of these are insoluble within the electrolyte, leading them to deposit on the electrode, in turn sterically hindering further lithiation of other polysulfide species and eliminating themselves from the battery charge/discharge cycle.<sup>43</sup> Moreover,  $\text{Li}_2\text{S}$  is also electronically insulating, serving to exacerbate the issues previously mentioned.<sup>18</sup> Thus, it is vitally important for us to improve our understanding of how lithiated polysulfide decomposition takes place and in what ways it can interfere with additional side reactions.

In order to understand the way in which a PS molecule behaves in an electrochemical environment and within an electrolyte medium, we have to first comprehend its behavior in the gas phase, or without effects capable of influencing its behavior, such as solvent interactions. Then we add implicit solvents to determine how their properties influence the stability and favorability of the PS decomposition products and reactions. Table 2 (below) summarizes these results. Note that the  $\text{Li}_2\text{S}_8$  molecule can conform to either a ring or linear form, as mentioned in the Introduction, with the solvent environment directly affecting the lowest-energy configuration. For the sake of simplicity, the calculations in Table 2 are performed using the linear values; the ring data is further examined later on within this chapter, and shows identical trends. In every case the lowest multiplicities correspond to the molecular structures with the lowest-energy.

For applicable reactions, this data shows good agreement with other computational studies of PS decomposition.<sup>44</sup>

**Table 2.** PS bond dissociation energies obtained from B3PW91/6-311++G(p,d) calculations

Reactions	Bond Dissociation Energies (eV)					
	Gas-Phase		EC Solvent		DOL Solvent	
	$\Delta E$ (0K)	$\Delta G$ (298K)	$\Delta E$ (0K)	$\Delta G$ (298K)	$\Delta E$ (0K)	$\Delta G$ (298K)
$\text{Li}_2\text{S}_8 \rightarrow 2\text{Li}^+ + \text{S}_8^{-2}$	14.11	13.51	0.45	-0.15	1.74	1.14
$\text{Li}_2\text{S}_8 \rightarrow 2\text{Li} + \text{S}_8$	7.02	6.37	8.85	8.24	8.39	7.76
$\text{Li}_2\text{S}_8 \rightarrow \text{LiS} + \text{LiS}_7$	2.43	1.94	2.05	1.55	2.07	1.56
$\text{Li}_2\text{S}_8 \rightarrow \text{LiS}_2 + \text{LiS}_6$	0.99	0.48	1.20	0.65	1.15	0.61
$\text{Li}_2\text{S}_8 \rightarrow \text{LiS}_3 + \text{LiS}_5$	1.28	0.79	0.87	0.33	0.81	0.30
$\text{Li}_2\text{S}_8 \rightarrow 2\text{LiS}_4$	0.31	-0.24	0.78	0.29	0.68	0.16
$\text{Li}_2\text{S}_8 + 2\text{Li} \rightarrow \text{Li}_2\text{S} + \text{Li}_2\text{S}_7$	-3.56	-3.43	-5.53	-5.39	-5.18	-4.85
$\text{Li}_2\text{S}_8 + 2\text{Li} \rightarrow \text{Li}_2\text{S}_2 + \text{Li}_2\text{S}_6$	-5.63	-5.38	-6.02	-5.92	-5.64	-5.51
$\text{Li}_2\text{S}_8 + 2\text{Li} \rightarrow \text{Li}_2\text{S}_3 + \text{Li}_2\text{S}_5$	-5.32	-5.17	-6.19	-6.09	-5.78	-5.65
$\text{Li}_2\text{S}_8 + 2\text{Li} \rightarrow 2\text{Li}_2\text{S}_4$	-6.95	-6.69	-6.28	-6.14	-6.15	-5.98
$\text{S}_8^{-2} \rightarrow \text{S}_1^{-1} + \text{S}_7^{-1}$	0.48	0.10	2.06	1.71	1.91	1.54
$\text{S}_8^{-2} \rightarrow \text{S}_2^{-1} + \text{S}_6^{-1}$	-0.85	-1.32	1.11	0.66	0.88	0.41
$\text{S}_8^{-2} \rightarrow \text{S}_3^{-1} + \text{S}_5^{-1}$	-1.33	-1.87	0.78	0.24	0.52	-0.03
$\text{S}_8^{-2} \rightarrow 2\text{S}_4^{-1}$	-1.39	-1.93	0.57	0.05	0.34	-0.18

From calculations in the gas phase, several observations can be made. First, every decomposition product is most stable with a (-1) charge (radical anions) rather than neutral or (-2) (dianions) save the  $\text{S}_8$  molecule, which prefers the dianion state. This

result is intriguing since the  $S_8^{-2}$  molecule does in fact favor decomposition within the gas phase, especially via the breaking of its middle sulfur bond. Originally, we assumed that the delithiation reaction occurred first, followed by subsequent polysulfide fragmentation, but in the gas phase this is certainly not the case. While this pathway has a smaller energy barrier within solvent, AIMD simulations of the  $Li_2S_8$  molecule in the three solvents which are discussed in this paper did not produce any decomposition without inclusion of the lithium metal surface, even for more than 20 picoseconds of simulation. Because of this, we are able to conclude that the main pathway of  $Li_2S_8$  fragmentation far from the anode does not include delithiation.

For PS molecules within the bulk solvent (those not experiencing direct interaction with the additional lithium atoms from the anode surface), decomposition is still seen within AIMD simulations of the anode, although this occurs at a much slower rate than what transpires at the lithium surface. While there is minimal precedent for this transpiring within the gas phase, charge transfer from the lithium surface to the electrolyte in anode simulations, something which has been confirmed through the use of Bader charge analysis, helps create an environment that is favorable for polysulfide dissociation. It is important to note, however, that even through the use of gas-phase data,  $Li_2S_8$  reduction to  $Li_2S_6$  ( $Li_2S_8 \rightarrow Li_2S_6 + S_2$ ), the first step in the conventional decomposition chain, is a thermodynamically favorable process, with  $\Delta G_{rxn}$  equal to -0.28 eV. Furthermore, the cleaving of the middle sulfur bond in the polysulfide is also feasible, as per Table 2.



Undoubtedly the most favorable polysulfide reaction pathway involves the reaction of additional lithium atoms from the surface with the lithiated polysulfide species. From gas phase calculations it is seen that the most thermodynamically favorable reaction is the cleaving of the middle sulfur bond, but each of these reactions is in fact very capable of happening (Table 2). The trend of increasing favorability with increasing PS fragment symmetry is broken by the formation of  $\text{Li}_2\text{S}_6$ , where both the free energy and enthalpy of the reaction are larger than the corresponding  $\text{Li}_2\text{S}_5$  values. A related trend is also observed in the data for reactions within the bulk solvent. This indicates that the configuration is in fact very stable for the lithiated polysulfides, giving credence to the reaction progression given near the start of this section ( $\text{Li}_2\text{S}_8 \rightarrow \text{Li}_2\text{S}_6 \rightarrow \text{Li}_2\text{S}_4 \rightarrow \text{Li}_2\text{S}_2 \rightarrow \text{Li}_2\text{S}$ ). Vijayakumar et al. indicate results which further support these assumptions, demonstrating via mass spectrometry the existence of  $\text{Li}_2\text{S}_8$ ,  $\text{Li}_2\text{S}_6$ , and  $\text{Li}_2\text{S}_4$ , in addition to  $\text{S}_8^{-2}$  and even clusters of polysulfides (containing more than two lithium atoms).

As shown in the Table 2 results, when the lithiated polysulfide molecule underwent simulation with an implicit solvent exhibiting dielectric properties similar to those of EC, it was made clear that ionic delithiation is substantially more likely to transpire, especially within the bulk solvent, whereas the neutral delithiation reaction continue to be highly unfavorable. This is in response to the stabilizing effect solvent has on dissipating the charges, which is the clear difference between these numbers and those seen within the gas phase. Near the surface of the anode, where extra lithium is present,  $\text{Li}_2\text{S}_8 + 2\text{Li}$  reactions are once again very favorable, despite the trend between

these reactions (Table 2) and those seen in the gas phase being much less pronounced. In that environment, there was an increase of 95% for the reaction energies when breaking one of the “end” sulfur-sulfur bonds instead of a “middle,” while the data from the EC calculations indicated an increase of only 14%. In addition, no evidence suggests a  $\text{LiS}_6$  or  $\text{Li}_2\text{S}_6$  molecule experienced unusual stability in the solvent, and in the AIMD simulations of the anode this has been confirmed – no clear transition into a  $\text{Li}_2\text{S}_6$  species exists throughout the decomposition process. Similarities of the reaction energies for  $\text{Li}_2\text{S}_8 + 2\text{Li}$  (again, shown in Table 2) agree with the AIMD simulation observations, indicating that the PS chain rupture point is random, meaning that any of the possible reactions have approximately equal favorability.

For  $\text{Li}_2\text{S}_n$  in EC, lithium dissociation is likely as long as  $n$  is greater than 2, i.e.,  $\text{Li}_2\text{S}_3$  going to  $\text{Li}^+ + \text{LiS}_3^{-1}$  is thermodynamically favorable. For all polysulfide species that are of the form  $\text{LiS}_n$ , the most favorable charge state is the dianion (-2), signifying that even for lithiated polysulfides with shorter chains ( $n$  less than 8), the delithiation reaction is still likely to occur. Because the dielectric constant of both DME and DOL is very similar, the reaction energies calculated for polysulfide species in these solvents were virtually the same. The polysulfide decomposition energies calculated in DME (not shown) were on average 1% lower than the DOL results for the same reactions (seen in Table 2), so in an effort to minimize redundancy this data is omitted from the thesis. Both DME and DOL are unreactive in the presence of the polysulfide and lithium anode over this timeframe, and these observations seem to be confirmed by the reaction energy calculations. Nevertheless, polysulfide surface reactions continue to be energetically

favorable, and even several Å from the surface, AIMD results still demonstrate decomposition of the PS molecule as a result of charge transferred from the anode to the electrolyte. The solvents tested (DME, DOL, and EC) have reduction potentials of -1.68, -1.48, and -1.46 V, respectively.<sup>36</sup> As a result of the small differences between the three, there appears to be no relationship between the solvent reduction potentials and the calculated results.

To further examine PS behavior at the lithium surface, AIMD calculations were executed by adding a linear or ring  $\text{Li}_2\text{S}_8$  molecule near to the Li surface and utilizing the salt/solvent mixtures which were detailed within the preceding section. Based on the results from the earlier solvent/salt simulations, the DOL/DME system seems to be the most viable candidate for simulating PS behavior near the anode. Understanding this interaction is critical to engineering better Li-S batteries which avoid the pitfalls of self-discharge. It should be noted that polysulfide shuttle, which brings the long-chain sulfur species from the cathode to the anode, is not a desirable effect, and while there are many proposed solutions to this problem, as of yet all lithium sulfur cells experience some degree of PS shuttle. For the first iteration of PS simulation at the anode, one molecule of  $\text{Li}_2\text{S}_8$  was added to the DOL/DME solvent mixture, corresponding to a concentration of 1M. A zoomed-in image of the electrolyte can be seen on Figure 22.

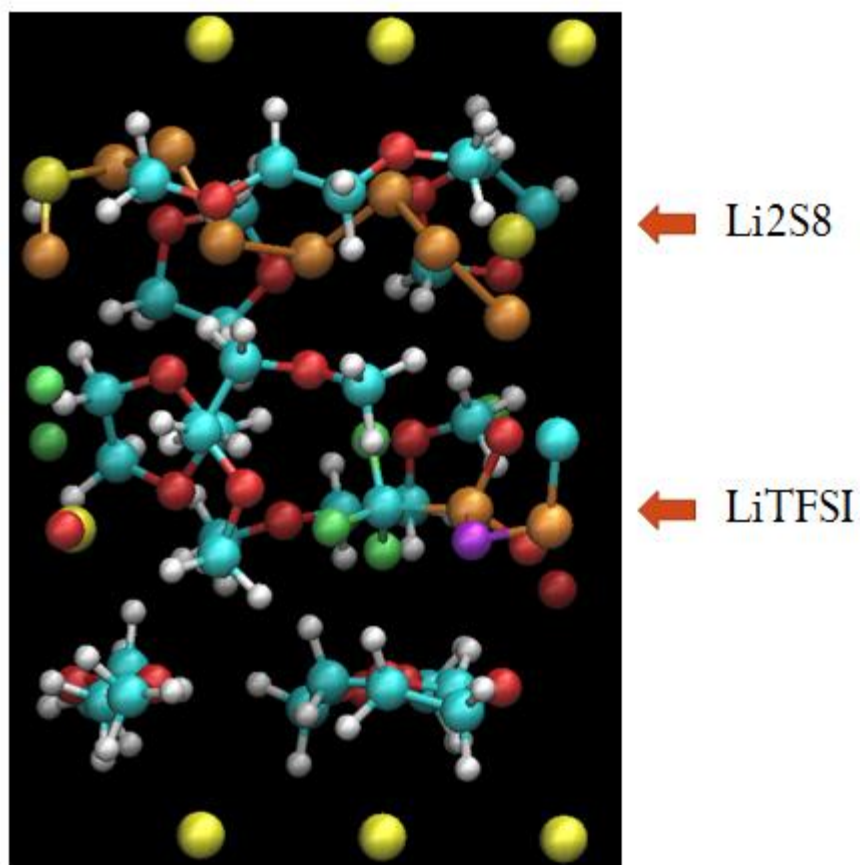


**Figure 22.** DOL/DME, 1M LiTFSI, 1M PS at 0ps. Color key: red, oxygen; white, hydrogen; blue, carbon; yellow, lithium; orange, sulfur; purple, nitrogen; green, fluorine

Within 50 fs the PS molecule begins to decompose, as seen in Figure 23, showing the simulation after 100 fs.

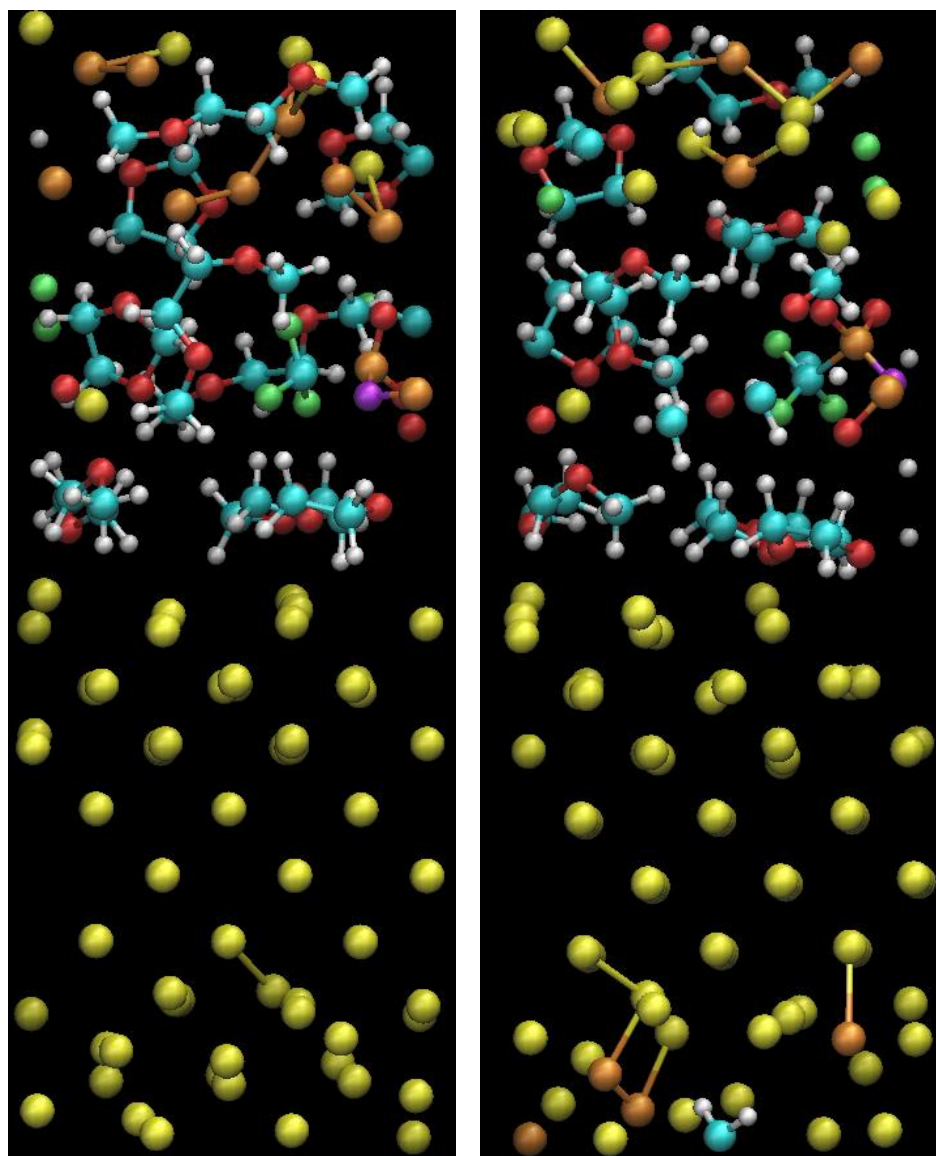


**Figure 23.** Left: DOL/DME, 1M LiTFSI, 1M PS at 100 fs. Right: after 4.0 ps (end of simulation). Color key: red, oxygen; white, hydrogen; blue, carbon; yellow, lithium; orange, sulfur; purple, nitrogen; green, fluorine

Once the PS has fragmented, the  $S_2$  and  $S_3$  molecules make their way to the anode surface, where they undergo further reduction. After 1 ps, the largest remaining sulfur group is diatomic, and by the end of the 4 ps simulation, none of the original S-S bonds have remained intact. It should also be observed that the lithium metal surface has

been severely disrupted due to the PS decomposition. Comparing the top and bottom lithium surfaces gives a good indication of the effect PS decomposition can have on surface structure and roughness, and by extension, potential dendrite formation. Meanwhile the salt begins to decompose at around 1.5 ps via the cleaving of a C-S bond, and both fragments survive until the end of simulation. This behavior will be examined in more detail later on when higher molarity PS systems are considered, but it is worth noting that not only does the salt in this simulation take longer to decompose, but that the fragments are less reactive and less inclined to move to the anode surface. This seems to be due to the passivating effect of the PS on the lithium metal surface, even when the LiTFSI molecule is located away from the PS species. The solvent undergoes no reactions over the course of this simulation.

Next, the concentration of PS was increased to 2M in order better understand the passivation effect, this time at both lithium faces as shown in Figure 24. Care was taken to keep the salt molecule in the same position within the vacuum slab during simulation using different PS molarities.

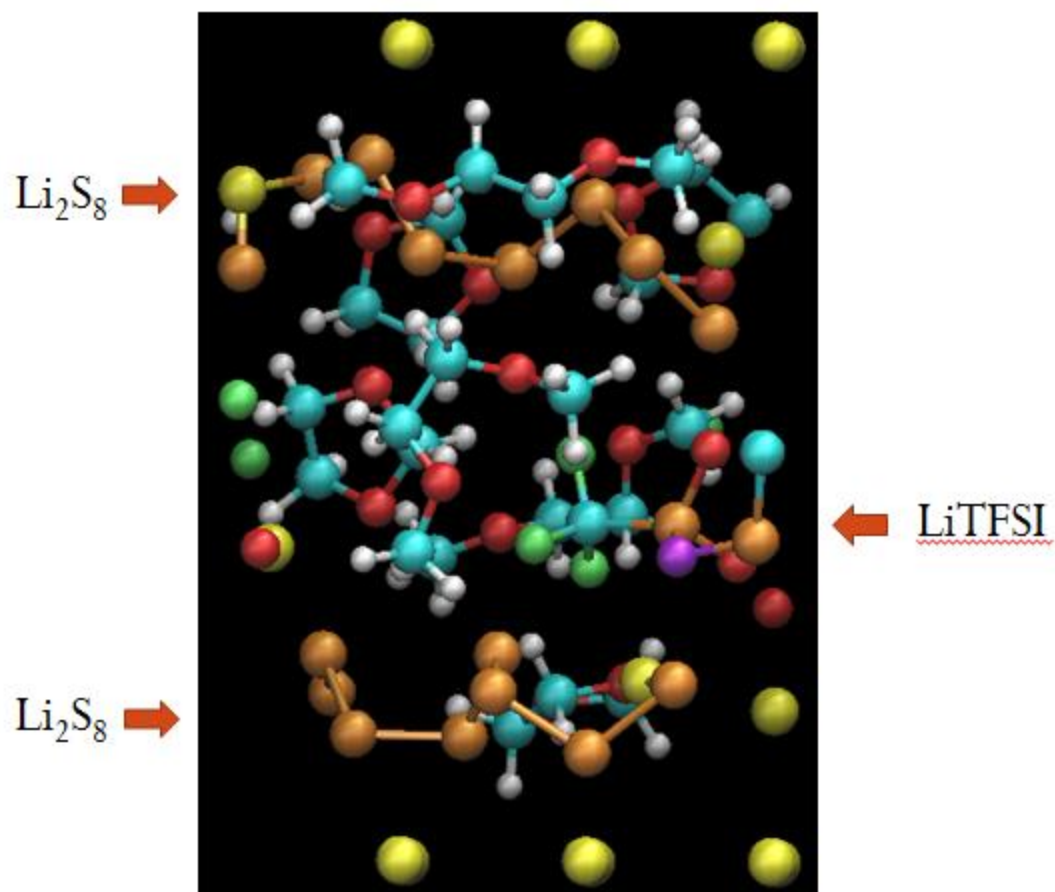


**Figure 24.** DOL/DME, 1M LiTFSI, 2M PS at 0ps. Color key: red, oxygen; white, hydrogen; blue, carbon; yellow, lithium; orange, sulfur; purple, nitrogen; green, fluorine

The results of this simulation are shown below in Figure 25.

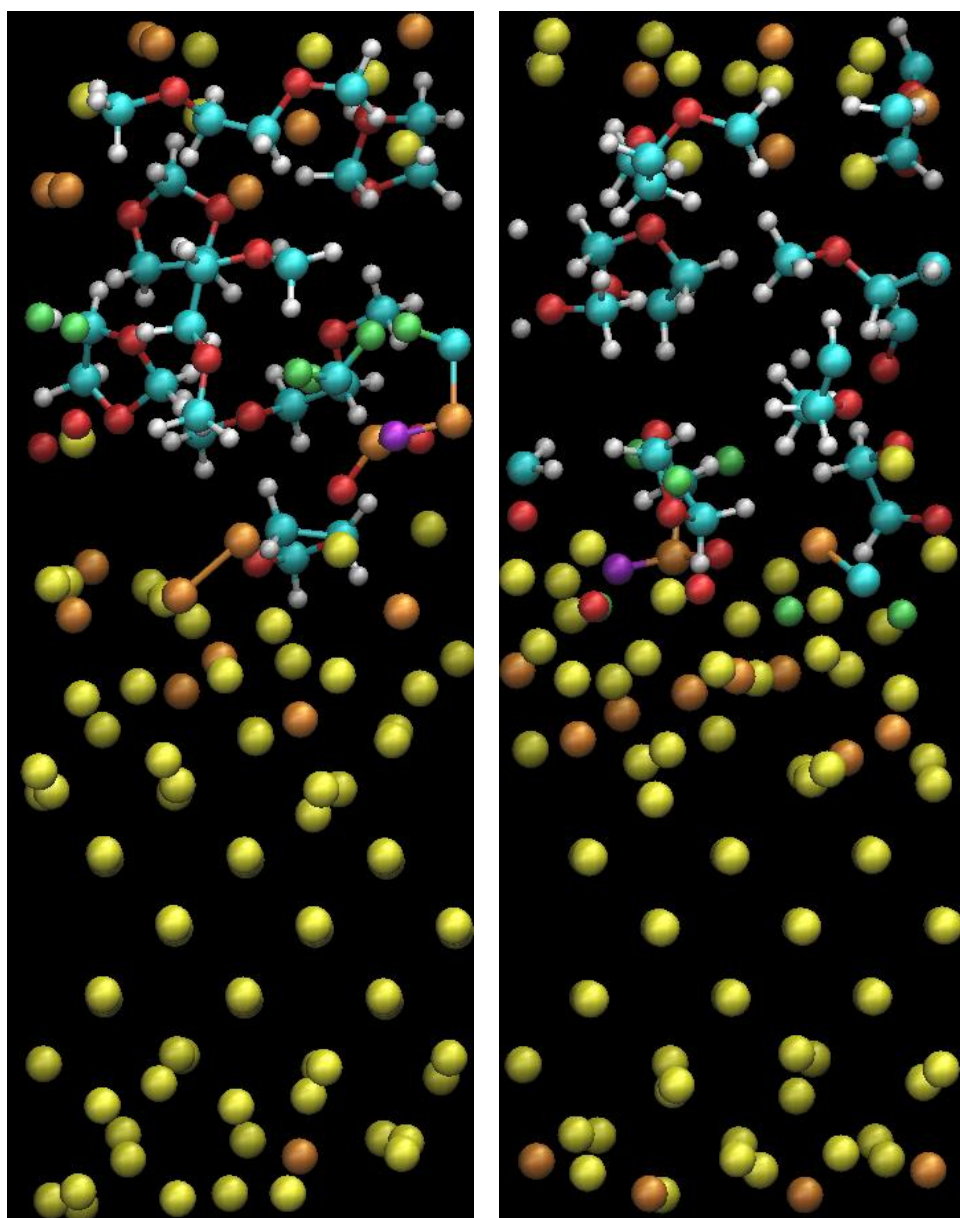


**Figure 25.** Left: DOL/DME, 1M LiTFSI, 2M PS at 500 fs. Right: after 9.0 ps (end of simulation). Color key: red, oxygen; white, hydrogen; blue, carbon; yellow, lithium; orange, sulfur; purple, nitrogen; green, fluorine

As we can see, both polysulfide molecules completely decompose, again very rapidly (within 50 fs). By 500 fs the PS is almost entirely fragmented (one  $S_2$  molecule remains), and these fragments begin to diffuse into the lithium bulk. After 1 ps the salt



molecule has split via an N-S bond, and the resulting  $\text{SO}_2\text{CF}_3$  group survives until 4.2 ps, when the C-S bond breaks. This is followed by partial defluorination of the  $\text{CF}_3$  group (4.5 ps), resulting in a CF group which recombines with the  $\text{SO}_2$  fragment. This molecule lasts until 6.6 ps, at which point it loses its final fluorine atom. By the 9.0 ps mark, this species has decomposed, leaving only the sulfur and carbon bonded; the remaining atoms are “loose” at the lithium surface.

The polysulfide effect on the anode surface is more pronounced in the 2M case due to both the upper and lower surfaces of the vacuum slab absorbing sulfur, but the nature of the anode surface is still rather obscure. It appears that the sulfur-lithium interactions at the surface do not follow anything like covalent bonding behavior, but there does seem to be a sort of amorphous characteristic of the layer. This may be due in part to the fact that the amount of sulfur needed to make a stoichiometric  $\text{Li}_2\text{S}$  surface is not met in these simulations. However, we can get an idea of the interconnections occurring within the anode surface by defining any sulfur atom within 2.6 angstroms of a lithium atom as “bonded” to it; this is the calculated distance between lithium and sulfur in an  $\text{Li}_2\text{S}$  molecule.<sup>45</sup> Figure 26 below shows the system at 2.3 ps with sulfur “bonds” added.

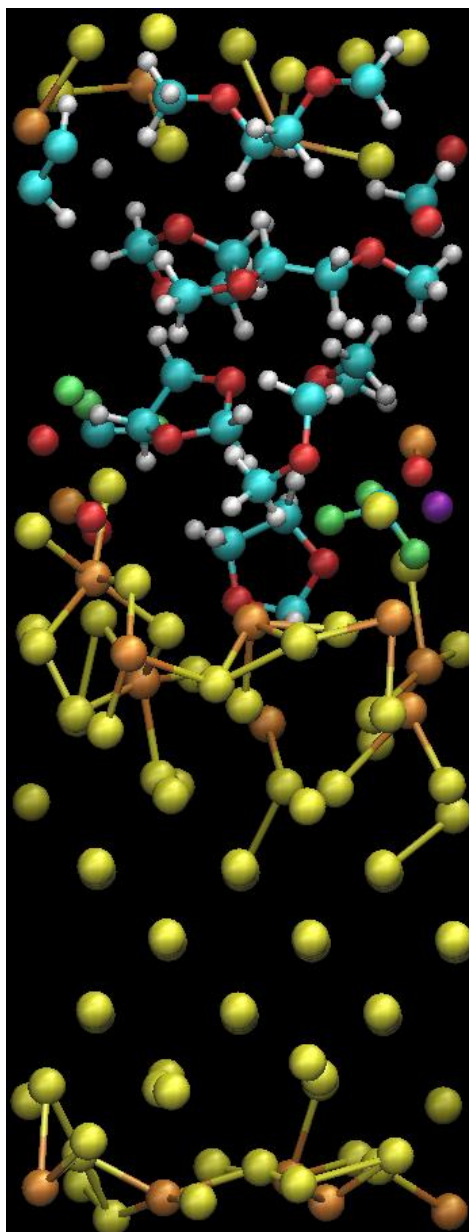


**Figure 26.** DOL/DME, 1M LiTFSI, 2M PS at 2.3 ps. Color key: red, oxygen; white, hydrogen; blue, carbon; yellow, lithium; orange, sulfur; purple, nitrogen; green, fluorine

From this exercise we see that practically every sulfur atom is within 2.6 angstroms of at least one lithium atom, and for some this coordination number is as high as four. These interactions help lead to the large increase in surface roughness that can

be seen by comparing the simulations of DOL/DME, 1M LiTFSI with and without the presence of PS species, as seen in Figure 27.

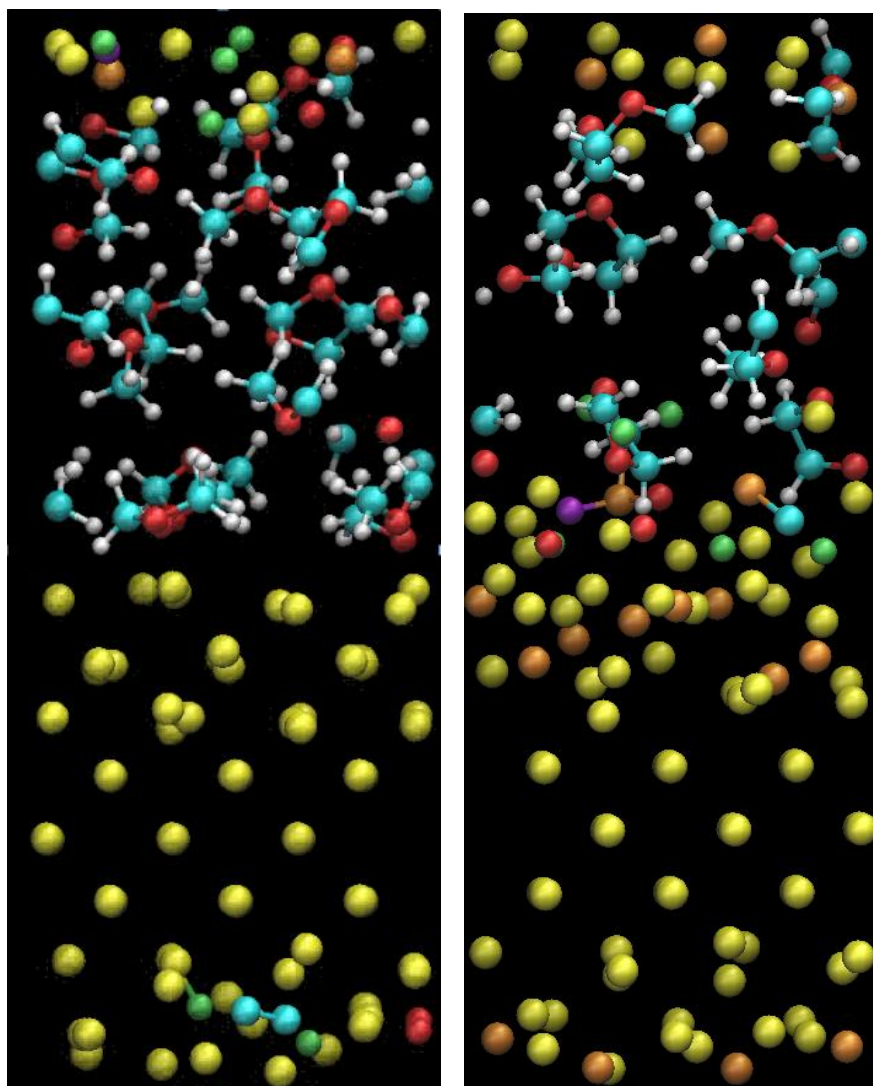


**Figure 27.** Left: DOL/DME, 1M LiTFSI at 9.2 ps. Right: DOL/DME, 1M LiTFSI, 2M PS after 9.0 ps. Color key: red, oxygen; white, hydrogen; blue, carbon; yellow, lithium; orange, sulfur; purple, nitrogen; green, fluorine

With the addition of the PS molecules and their subsequent decomposition, the anode surface evolves quite dramatically. The intercalation of sulfur atoms into the

lithium bulk results in a volume expansion which leads to a lithium “surface” nearly three angstroms above the starting position of the lattice, while for the inert solvent molecules in Figure 27 (left), the surface atoms remain roughly in place. It should also be noted that in none of the AIMD simulations run over this timescale was there found an instance of either DOL or DME decomposition.

Finally, a three PS system was constructed and simulated to determine if a polysulfide in the bulk solvent, shielded from the lithium surface by other PS molecules, would still decompose. The initial system is shown in Figure 28.

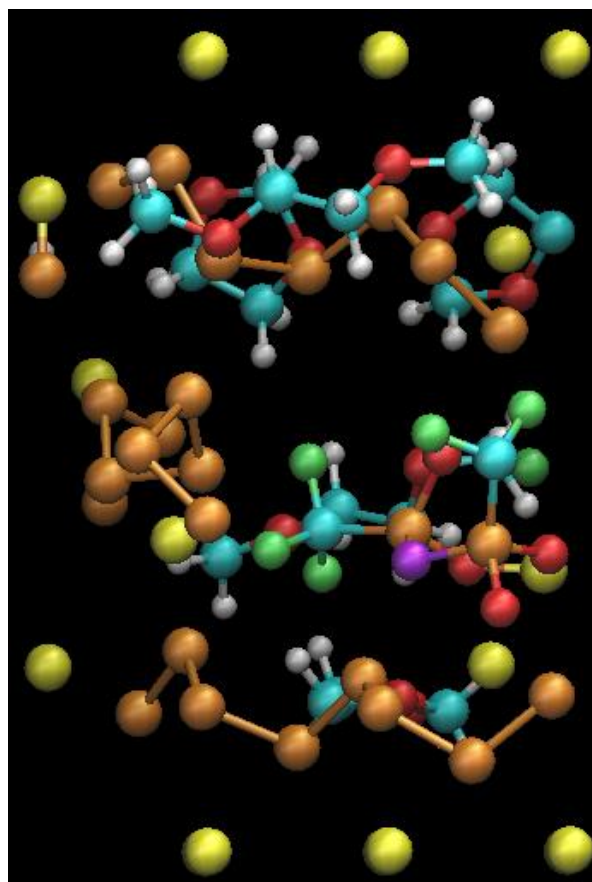


**Figure 28.** DOL/DME, 1M LiTFSI, 3M PS at 0ps. Color key: red, oxygen; white, hydrogen; blue, carbon; yellow, lithium; orange, sulfur; purple, nitrogen; green, fluorine

The simulation was run for 9.8 ps, and the results are shown in Figure 29 below, alongside the previous results for the 2M PS system.

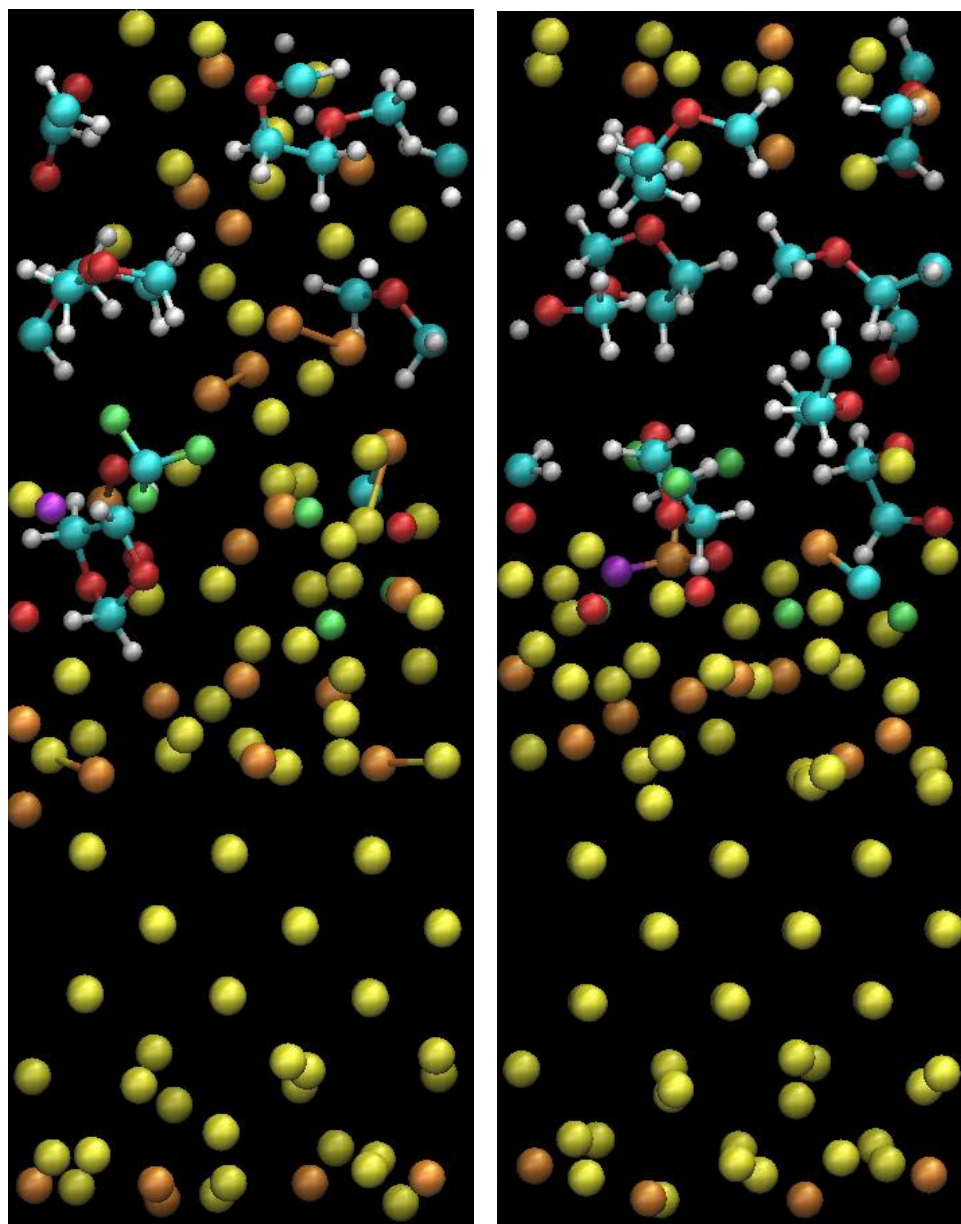


**Figure 29.** Left: DOL/DME, 1M LiTFSI, 3M PS at 9.8 ps. Right: DOL/DME, 1M LiTFSI, 2M PS after 9.0 ps. Color key: red, oxygen; white, hydrogen; blue, carbon; yellow, lithium; orange, sulfur; purple, nitrogen; green, fluorine

In the 3M PS case, all polysulfide molecules break within 70 fs, and while the molecule in the solvent bulk survives longer, it still succumbs to reduction by the lithium anode. For the bulk PS, an S-S bond is cleaved within 100 fs, resulting in  $\text{LiS}_3$  and  $\text{LiS}_5$  formation. These two molecules survive until around 2 ps, at which time they have both delithiated, and the  $\text{S}_5$  group has been reduced to  $\text{S}_2$  and  $\text{S}_3$ . Decomposition continues, but even as late as 8 ps, an  $\text{S}_3$  group remains in the bulk, and at the end of the simulation (9.8 ps) there are still  $\text{S}_2$  groups intact. The salt molecule enjoys similar stability, surviving until the 6.9 ps mark, at which time it fragments along a C-S bond. The  $\text{CF}_3$  group defluorinates soon after (7.2 ps), and later the carbon bonds to one of the many sulfur atoms at the surface, forming a C-S molecule which survives until the end of the simulation. The remainder of the salt stays intact despite being surrounded by lithium and sulfur in the bulk.

Perhaps the most dramatic difference between the 2M and 3M PS cases is seen in the behavior of the lithium atoms away from the anode surface. The presence of a polysulfide in the bulk seems to act as a bridge of sorts, allowing an upswell of lithium atoms. The nucleophilic PS decomposition fragments draw lithium upward, and the end result is a chain of lithium and sulfur that connects both the top and bottom portions of the vacuum slab. This may represent preliminary dendritic growth, or at least the tendency for lithium to migrate upward under certain conditions in the electrolyte.

Outside of the linear PS configuration used hitherto, the lithiated, long-chain  $\text{Li}_2\text{S}_8$  molecule can also take on a ring form, shown in Figure 30.

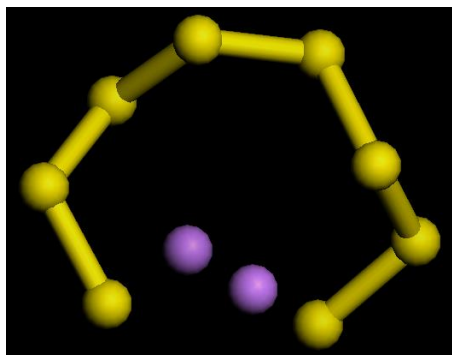


**Figure 30.** Ring configuration of  $\text{Li}_2\text{S}_8$ .

While the chemical formula may be the same for both configurations, the prevalence of either form is dependent upon the solvent environment and kinetic limitations. In order to examine any differences in stability or reactivity between the ring and linear configurations, three molecules of PS in the ring form (corresponding to 3M) were added to the earlier 3M PS simulation, replacing the linear PS molecules. The result is an electrolyte comprised of 3 molecules of DOL, 2 of DME, 1 of LiTFSI, and three of ring-form PS, as shown in Figure 31.

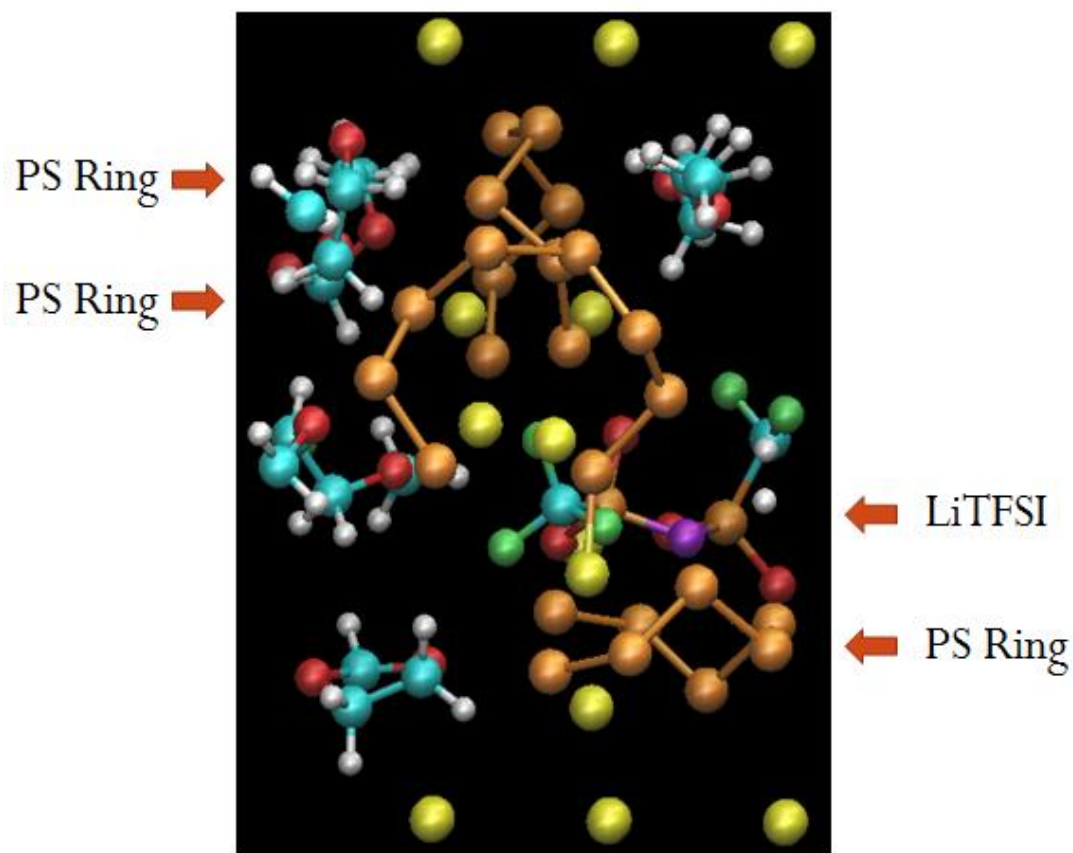


**Figure 31.** DOL/DME, 1M LiTFSI, 3M PS at 0 ps. Color key: red, oxygen; white, hydrogen; blue, carbon; yellow, lithium; orange, sulfur; purple, nitrogen; green, fluorine

AIMD calculations were performed over 12.3 ps, with the final configuration of the system shown in Figure 32 below.



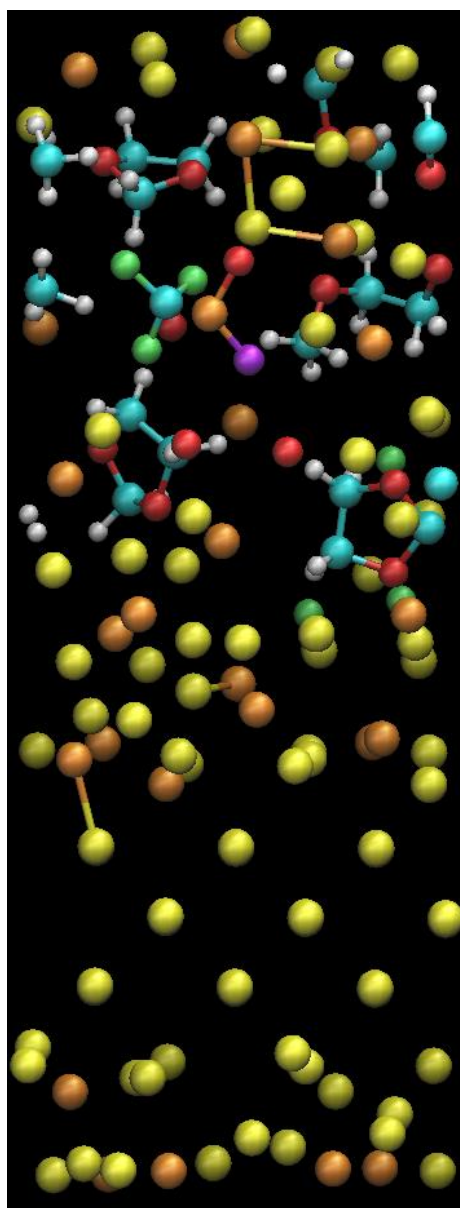


**Figure 32.** DOL/DME, 1M LiTFSI, 3M PS at 12.3 ps. Color key: red, oxygen; white, hydrogen; blue, carbon; yellow, lithium; orange, sulfur; purple, nitrogen; green, fluorine

Within 100 fs, every PS molecule has begun to decompose, and by 500 fs  $S_3$  groups are the largest PS fragments remaining. The loose sulfur atoms migrate to the lithium surface and begin to diffuse into the bulk. After 4 ps, the only surviving fragment

is one S<sub>2</sub> group. Meanwhile the salt enjoys comparative stability, lasting for 6.8 ps before decomposing via a C-S bond. Subsequent defluorination of the CF<sub>3</sub> group begins at 8.3 ps. By the conclusion of the simulation this fragment has completely decomposed, while the rest of the salt molecule remains intact. Compared to the 3M linear case, the differences found in the ring simulation are relatively minor. In both cases the solvent molecules did not decompose for the entirety of the experiment, the PS molecules began to decompose almost instantly, the bulk PS molecule experienced a slightly slower decomposition, and the salt decomposed at roughly the same time (6.9 ps and 6.8 ps for the linear and ring cases, respectively).

## **D2**

In addition to the three solvents mentioned above, D2 was also tested due to the positive experimental results shown by our collaborator Dr. Vilas Pol at Purdue University<sup>15</sup>. By adding this fluorinated ether to a DOL/LiTFSI salt system, the cell was shown to have a coulombic efficiency of more than 96% after 100 cycles, which far surpasses the results of typical Li-S electrolyte formulations. In order to replicate the parameters of the experiment, DOL and D2 were mixed at a 1:2 volume ratio, which corresponded to 3 molecules of each after adding one molecule each of PS and LiTFSI salt (both at 1M concentration). Figure 33 shows the electrolyte at the start of simulation.

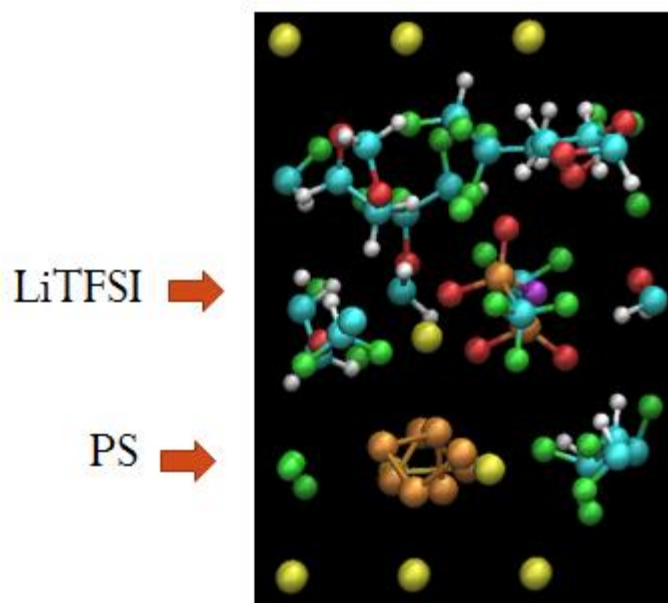


**Figure 33.** DOL/D2, 1M LiTFSI, 1M PS at 0ps. Color key: red, oxygen; white, hydrogen; blue, carbon; yellow, lithium; orange, sulfur; purple, nitrogen; green, fluorine

Once again, the PS molecule begins to decompose almost instantly (within 100 fs), while the salt begins to break after 4.7 ps via S-C bond cleavage. Figure 34 shows both the initial and final configurations of this system.

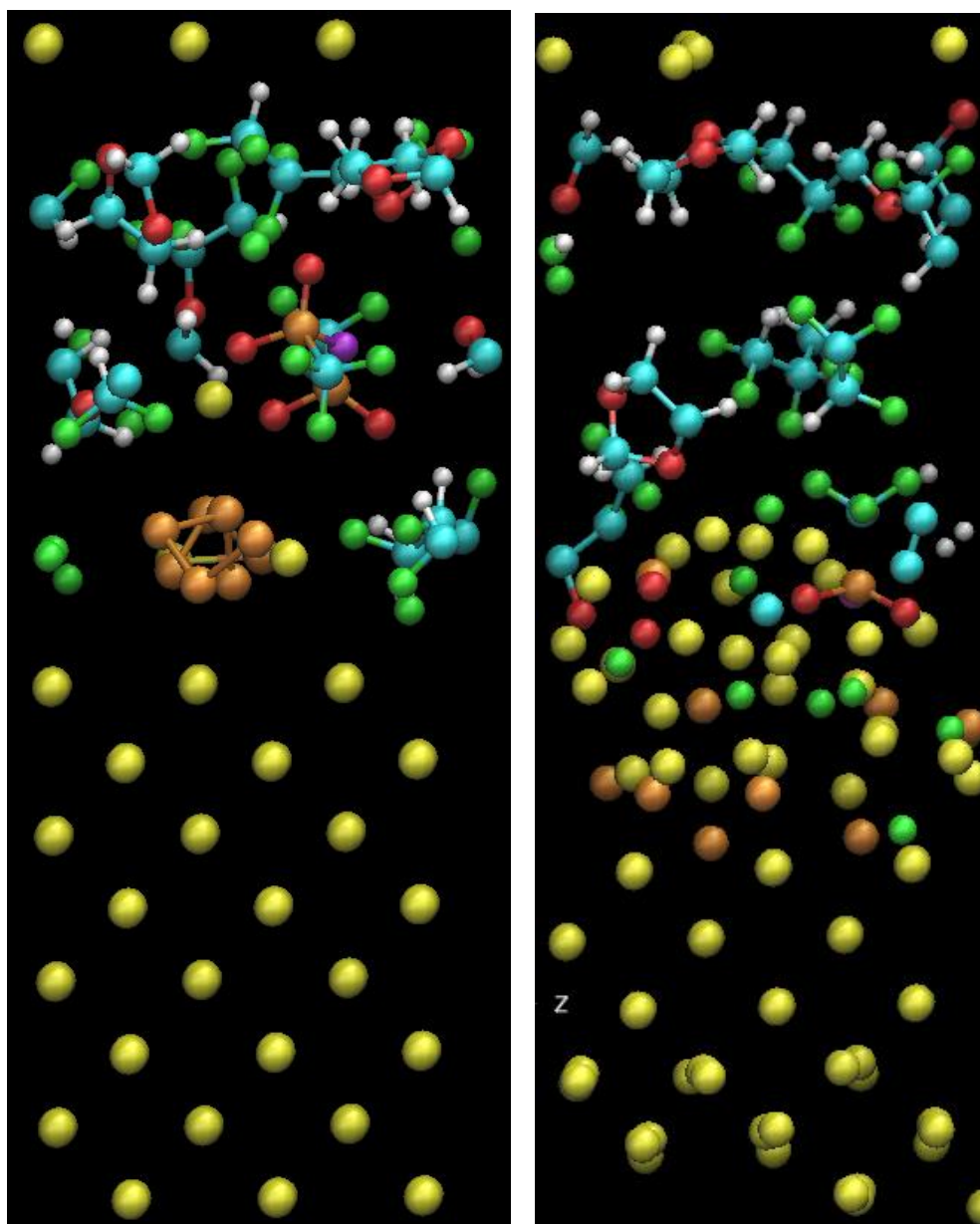


**Figure 34.** Left: DOL/D2, 1M LiTFSI, 1M PS at 0 ps. Right: After 17.9 ps. Color key: red, oxygen; white, hydrogen; blue, carbon; yellow, lithium; orange, sulfur; purple, nitrogen; green, fluorine

Again, we see the PS decomposition play the largest role in disturbing the lithium surface. Of interest is the fact that the eight sulfur atoms from the PS molecule all migrate into the lithium surface, while the sulfur atoms from the salt decomposition

(SO<sub>2</sub>) stay at the lithium surface, either stabilized by the oxygen atoms or less able to diffuse into the bulk due to steric limitations of the attached oxygen. The most intriguing part of this simulation, however, is the relative stability of the D2 molecules. While the bottommost D2 molecule began to defluorinate at 1.3 ps, the other two do not show such behavior, even near the lithium surface. This seems to indicate that the local PS decomposition has at least a minor effect on the D2 stability, perhaps due in part to the upheaval of lithium atoms at the anode surface. Compared to DME, the D2 does seem more reactive, but this drawback is potentially outweighed by its reported benefits, such as suppressing PS shuttling and producing higher coulombic efficiency.<sup>46</sup>

### **LiFSI**

In addition to changing the solvent composition, the use of an alternative salt, LiFSI, was also investigated. As stated in the introduction, LiFSI has seen use in Li-S systems as an alternative to the more traditional LiTFSI salt.<sup>25</sup> However, it has also shown promise in other battery chemistries, including LiFePO<sub>4</sub>/graphite<sup>47</sup> and Li/Si.<sup>48</sup> To better understand its role and impact in lithium-sulfur batteries, 1M LiFSI was added to a pure DME system and compared to the 1M LiTFSI counterpart. This system was chosen to replicate the conditions used by Qian's group, particularly the use of the pure DME instead of a solvent mixture. The 1M LiFSI case is shown below in Figure 35.

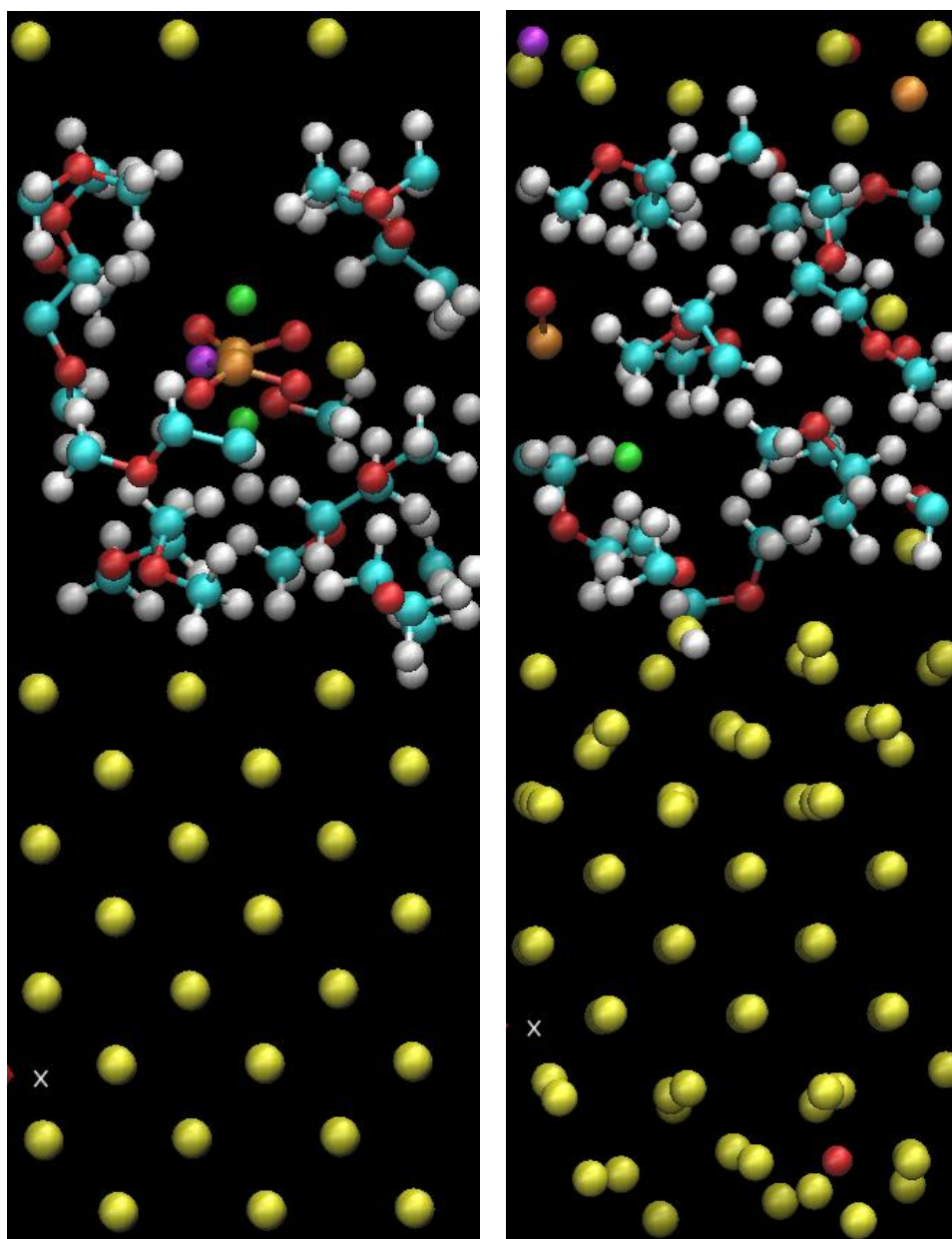


**Figure 35.** Left: DME, 1M LiFSI, at 0 ps. Right: After 13.4 ps. Color key: red, oxygen; white, hydrogen; blue, carbon; yellow, lithium; orange, sulfur; purple, nitrogen; green, fluorine

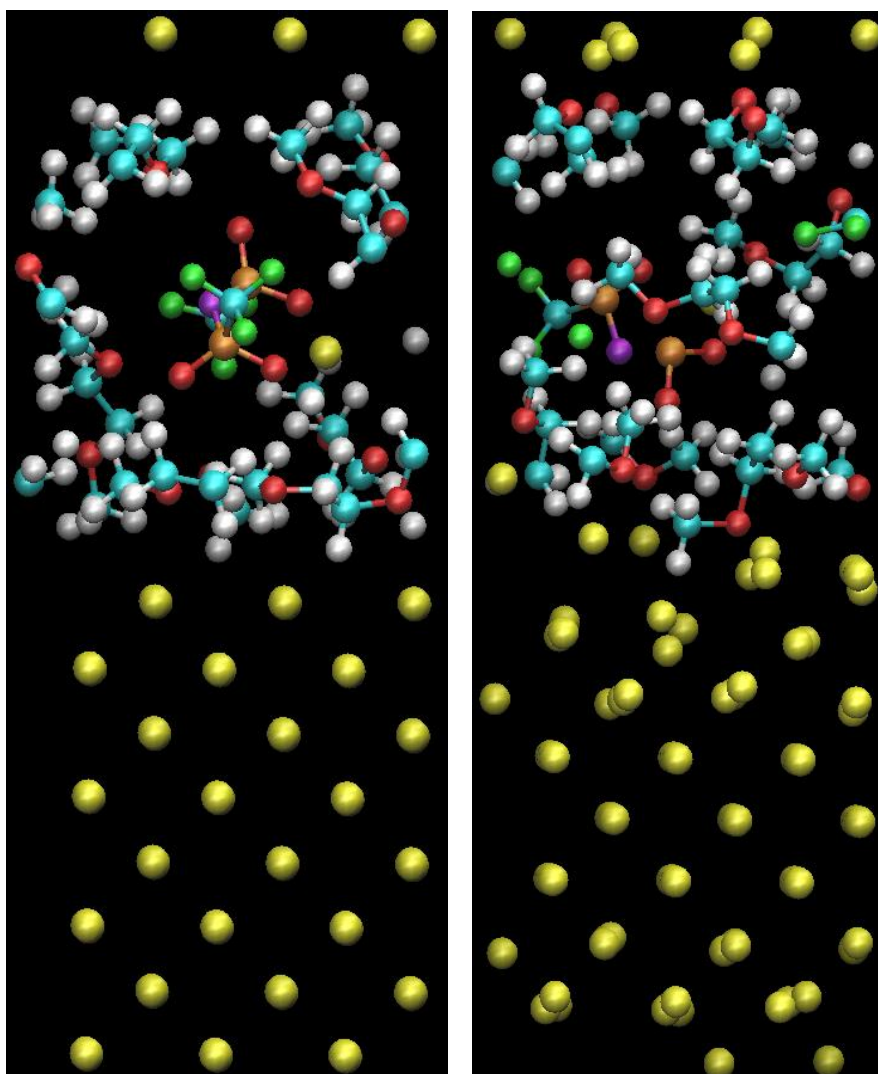


**Figure 36.** Left: DME, 1M LiTFSI, at 0 ps. Right: After 13.2 ps. Color key: red, oxygen; white, hydrogen; blue, carbon; yellow, lithium; orange, sulfur; purple, nitrogen; green, fluorine

As we can see, the salt molecule does not survive the duration of the simulation. At 1.8 ps it dissociates, and the resulting FSI fragment begins to defluorinate at 3.7 ps, finally losing the  $\text{SO}_2$  group after 4 ps. Eventually the rest of the salt decomposes as well, and by the end of the simulation only an  $\text{LiSO}_2$  fragment remains in the bulk, with the rest of the salt having migrated to the upper lithium anode surface and reduced. In order to

compare LiFSI and LiTFSI stability in the electrolyte, the LiFSI molecule was replaced by a LiTFSI molecule in the same system and at the same position within the vacuum slab. This is shown in Figure 36. In this case, the salt also decomposes by the breaking of an S-C bond at 5.1 ps, both fragments survive until the end of the simulation. Also, the salt does not dissociate, as was the case with the LiFSI simulation. This seems to indicate that there is a significant difference in both the reactivity and reduction pathways for the two salt molecules. For this reason, both salts were tested in explicit solvent simulations in order to determine their stability in DME away from the anode, with the same methodology as used in the case of the PS explicit solvent simulations. Over 16 ps, however, the LiFSI does not decompose, and neither does the LiTFSI. This indicates that the presence of the lithium anode is a major factor driving the salt reduction. In order to provoke a reaction, one electron was added to the LiFSI/DME explicit solvent system, using the same methodology discussed in the PS section. In this case, the LiFSI was made to decompose, but by the cleaving of an S-F bond instead of the lithium dissociation seen in the anode surface simulation. Instead, the fluorine atom first bonds to a hydrogen atom from one of the DME molecules, then bonds to the lithium at around 400 fs, forming an O-Li-F chain that survives until the end of the simulation, as seen in Figure 37.



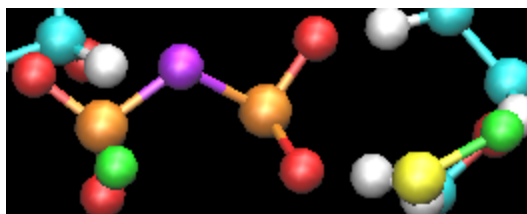


**Figure 37.** LiFSI molecule in DME at 16 ps, and after the addition of one extra electron

Because of the seemingly conflicting AIMD results, DFT calculations were performed using Gaussian analysis to determine the reaction energy and free energy of the dissociation of both the LiFSI and LiTFSI in implicit solvent DME and the Gas-Phase (no solvent). This was done by calculating the energy of the initial molecule and its charged products and subtracting the latter from the former. The LiTFSI results for energy of dissociation are shown in Table 3.

**Table 3.** LiTFSI energy of dissociation in gas-phase and DME

Solvent	Reaction E [eV]	Reaction G [eV]
Gas-phase	5.96	5.64
DME	0.75	0.43

The LiFSI results are seen in Table 4.

**Table 4.** LiFSI energy of dissociation in gas-phase and DME

Solvent	Reaction E [eV]	Reaction G [eV]
Gas-phase	5.77	5.44
DME	0.62	0.31

As can be seen from a brief comparison of these results, there is very little difference between the two. For the dissociation reaction in DME, there is a 28% reduction in the free energy of reaction between the LiTFSI and LiFSI, but neither is favorable. This seems to support the idea that the LiFSI is, in fact, stable far away from the anode surface, as is the LiTFSI, and as was seen in the explicit solvent results with DME. However, in order to be sure, energy calculations were made using explicit solvent systems. The energies of the salt and its decomposition products were all calculated in the presence of six DME molecules, and then the energy of the product systems were subtracted from those of the reactant. The final results in reaction energy between the implicit and explicit solvent calculations differed by only 5%, leading us to conclude that the previous results were in fact accurate, and that the real driving force in salt decomposition is not the solvent, but the presence of the lithium anode.

## CHAPTER IV

### HIGH MOLARITY SALT EFFECTS

While electrolytes containing 1M LiFSI or 1M LiTFSI have been heretofore examined, the use of higher molarity salts has been shown to produce some very positive results in lithium-sulfur batteries.<sup>11</sup> In Qian's work, an electrolyte consisting of 4M LiFSI and DME was found to enable high-rate cycling (with up to 99.1% Coulombic efficiency) of the lithium metal anode, in addition to inhibiting dendrite growth. This was attributed to increased Li-ion concentration within the electrolyte, as well as improved coordination of the solvent molecules. Using AIMD simulations, we are able to help provide a theoretical explanation for these encouraging experimental results by observing the differences between not only the low and high molarity salt cases, but also the differences between LiTFSI and LiFSI, which were shown to be experimentally dramatic.

To begin, we examine the 4M LiTFSI case, which is shown below in Figure 38. This molarity corresponds to four salt molecules for the volume of the vacuum slab used in these calculations.

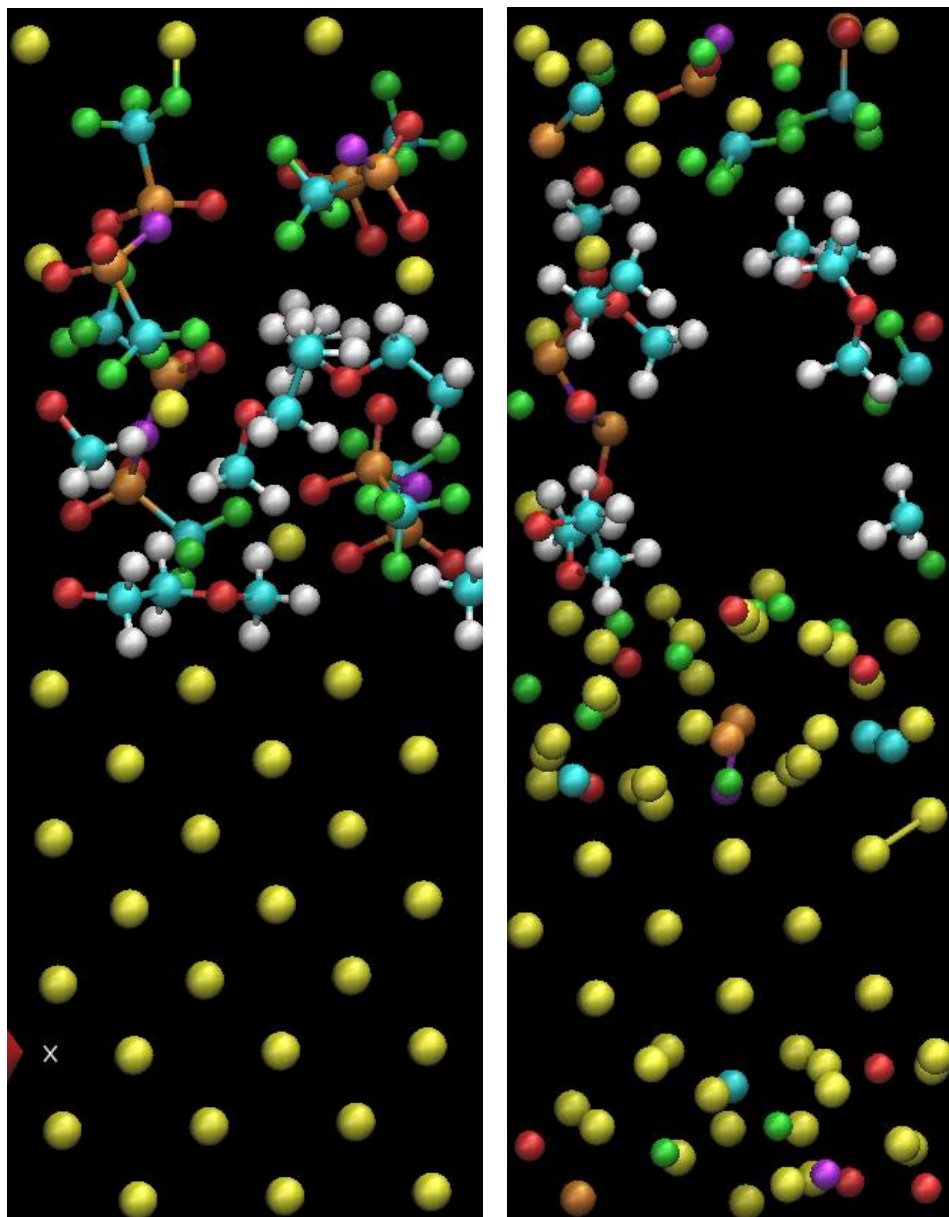


**Figure 38.** Left: DME, 4M LiTFSI, at 0 ps. Right: After 16.0 ps. Color key: red, oxygen; white, hydrogen; blue, carbon; yellow, lithium; orange, sulfur; purple, nitrogen; green, fluorine

This system is extremely unstable, with the salt molecules beginning to decompose within 20 fs. After 5 ps, both salt molecules at the top of the simulation have decomposed, and by the conclusion of the simulation all four salt molecules had reacted.

However, large fragments still remain, including  $\text{SO}_2\text{CF}_3$ ,  $\text{NSO}_2\text{CF}_3$ , and an entire salt molecule sans a  $\text{CF}_3$  group. No DME decomposition was observed over the course of this simulation. Thus, while the high molarity LiTFSI electrolyte is very prone to salt decomposition, the fragments remain large and survive the duration of the simulation.

This stands in sharp contrast to the 4M LiFSI case, shown in Figure 39 below.

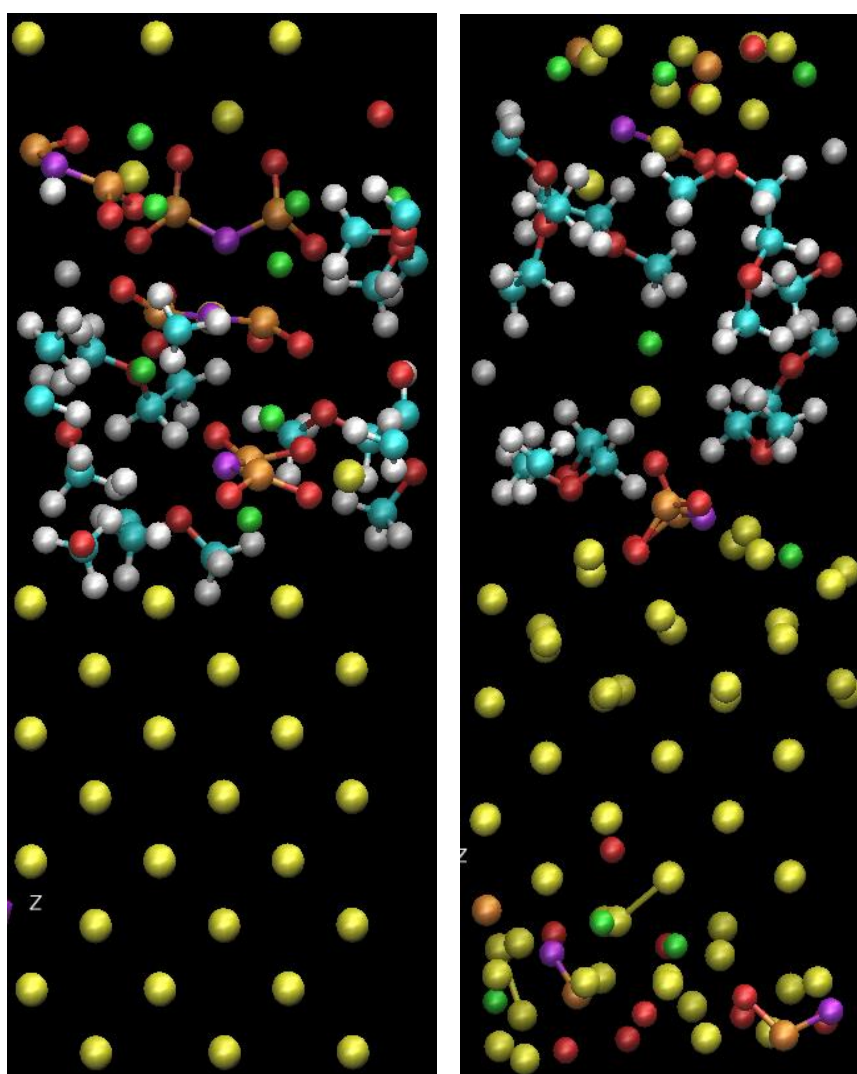


**Figure 39.** Left: DME, 4M LiFSI, at 0 ps. Right: After 16.0 ps. Color key: red, oxygen; white, hydrogen; blue, carbon; yellow, lithium; orange, sulfur; purple, nitrogen; green, fluorine

For this system, the topmost LiFSI molecule loses a fluorine atom within 150 fs, and by the 1.2 ps mark the next-highest salt molecule begins to fragment. After 5 ps, every salt molecule has reacted at least once. At the end of the simulation, the only large fragment remaining is the LiFSI molecule at the bottom of the vacuum slab, which has only lost one fluorine atom. On the whole, though, the LiFSI seems to undergo much more decomposition than the LiTFSI case; aside from the bottommost LiFSI molecule, the largest fragments are two NSO<sub>2</sub>, one NSO, and one SO group. Particularly for the fluorine atoms, the difference between the salts is dramatic. For the LiFSI, only one fluorine atom stays attached to the salt for the duration of the simulation, while for the LiTFSI, several whole CF<sub>3</sub> groups remain adhered.

In order to gain more insight into the behavior of the high molarity LiFSI case, Bader charge analysis was conducted on the atoms within each salt molecule to monitor the changes in charge associated with the breaking of bonds. The molecules are labeled from 1 to 4, with 1 being the topmost salt molecule in the initial configuration shown in Figure 39 (left), 2 being second from the top, etc. The results for molecule 1 are shown below in Figure 40.

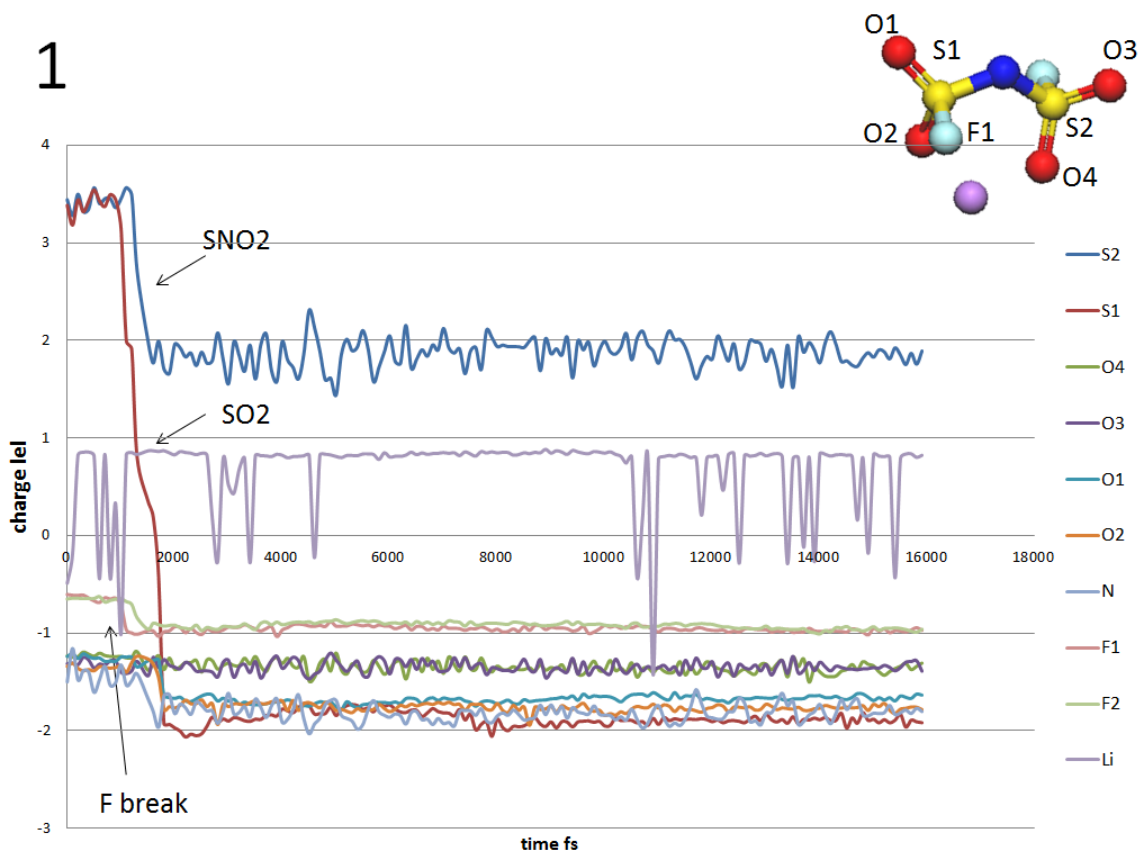


**Figure 40.** Charge analysis results for molecule 1

In Figures 41 and 42 the reactions for salt molecule 1 are shown in detail.

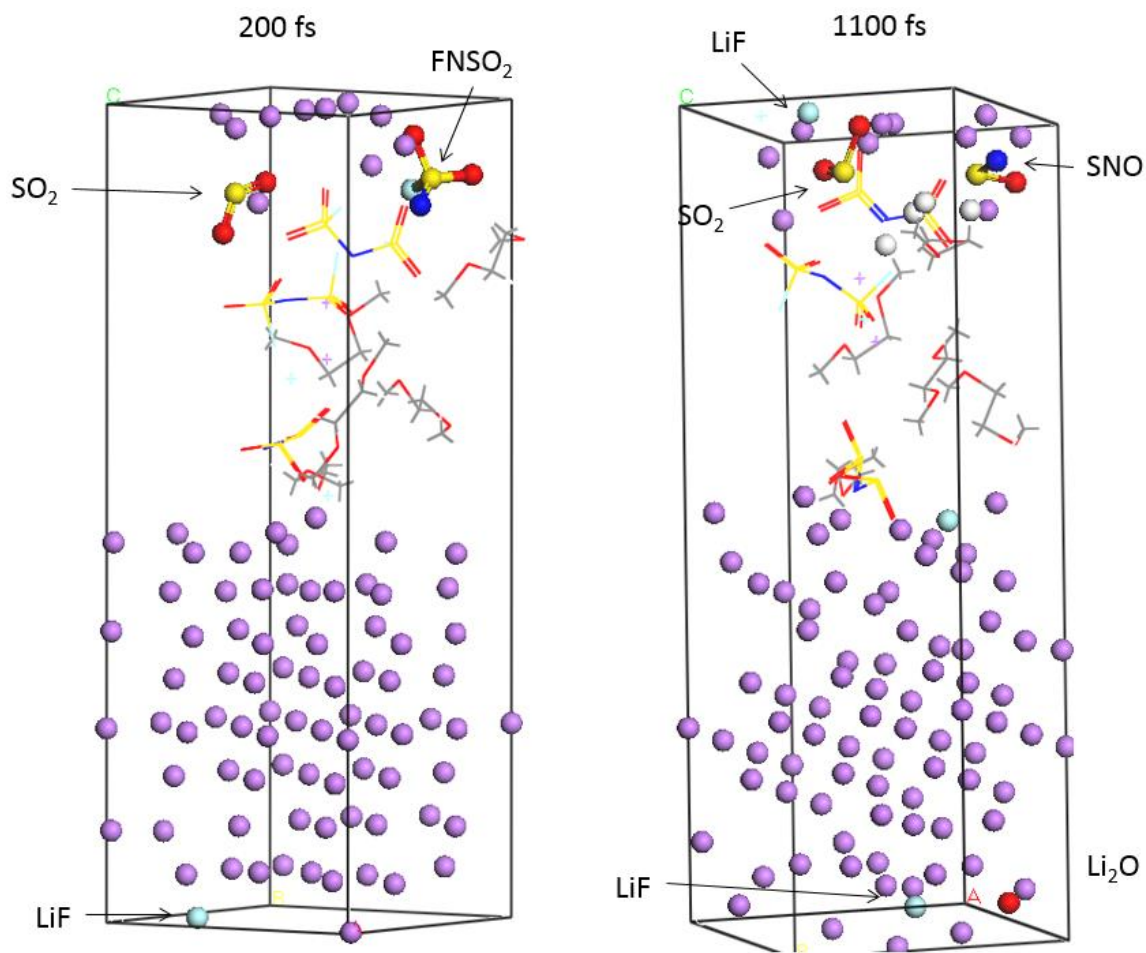


**Figure 41.** Left: DME, 4M LiFSI, at 200 fs, highlighting molecule 1. Right: After 1.1 ps. Color key: red, oxygen; white, hydrogen; blue, nitrogen; purple, lithium; yellow, sulfur; grey, carbon; teal, fluorine



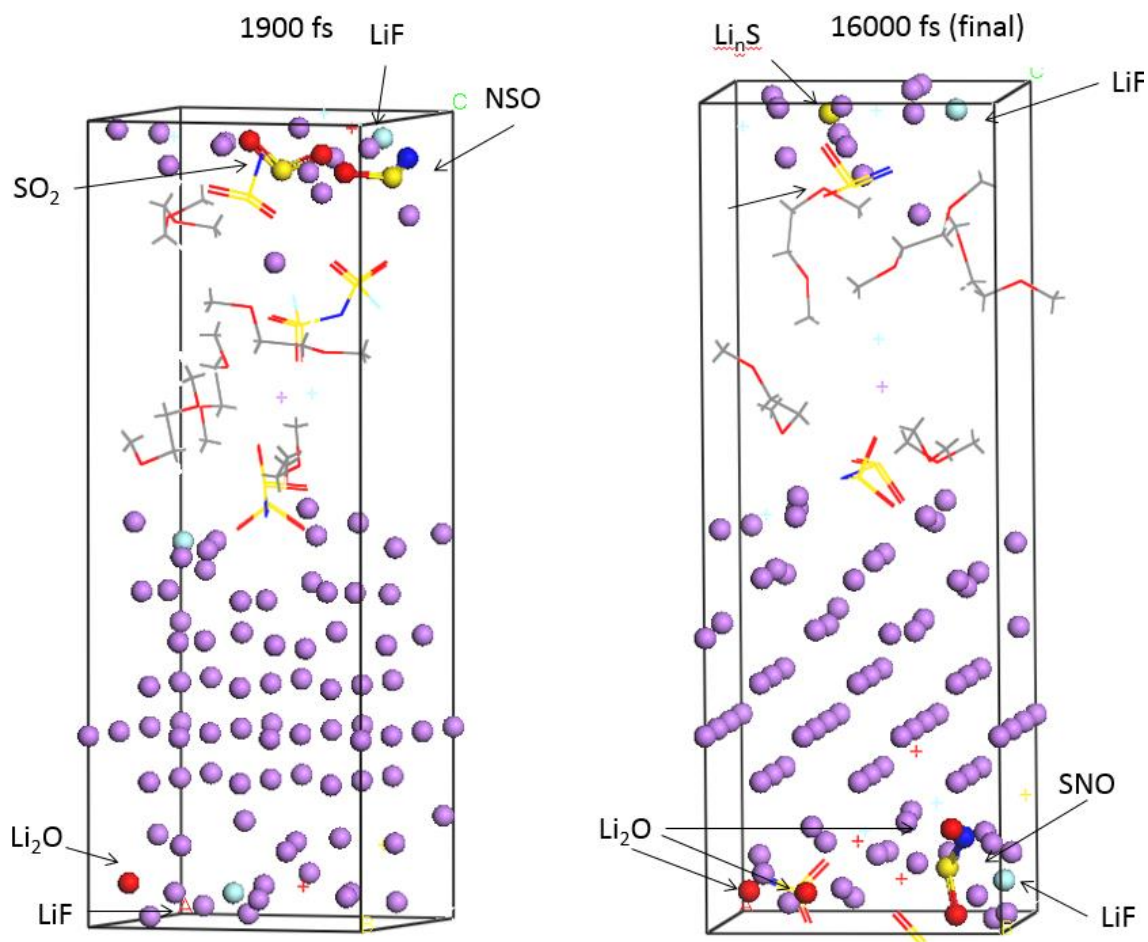


**Figure 42.** Left: DME, 4M LiFSI, at 1.9 ps, highlighting molecule 1. Right: After 16.0 ps. Color key: red, oxygen; white, hydrogen; blue, nitrogen; purple, lithium; yellow, sulfur; grey, carbon; teal, fluorine

For LiFSI molecule 2, the charge analysis results are seen below in Figure 43.

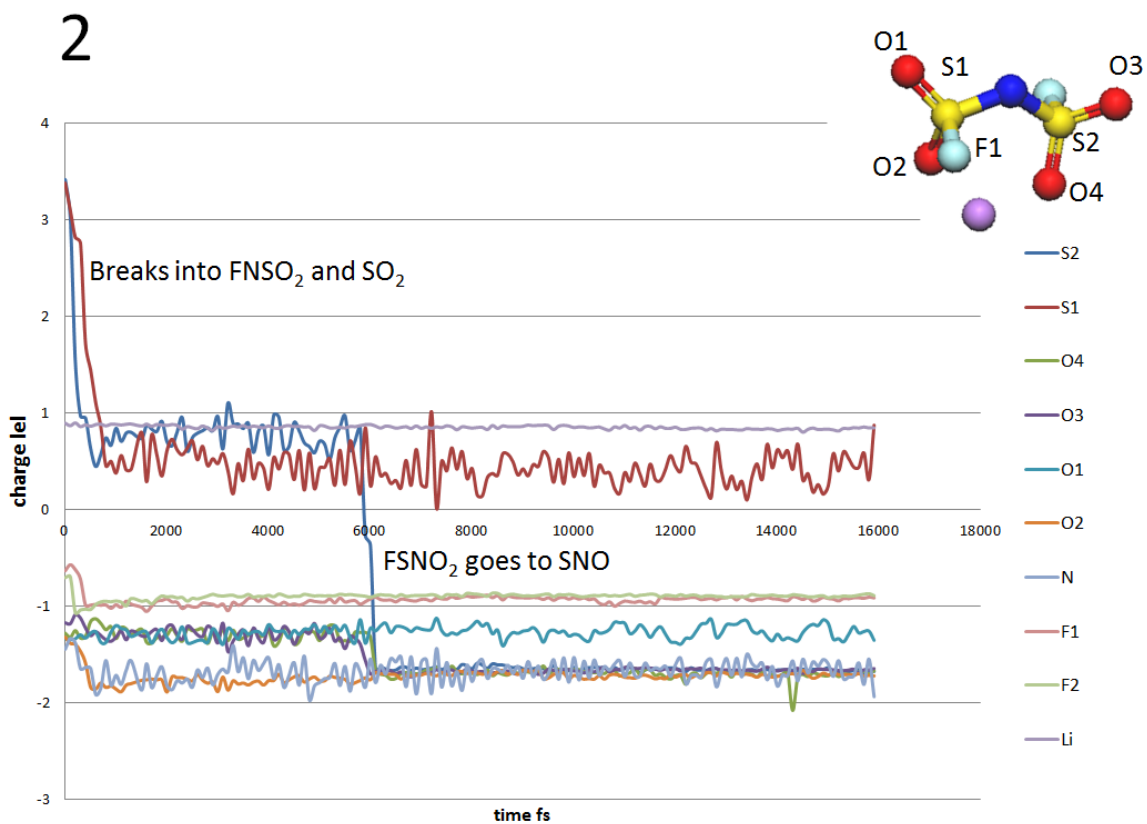


**Figure 43.** Charge analysis results for molecule 2

Figure 44 shows the reactions for this salt molecule.

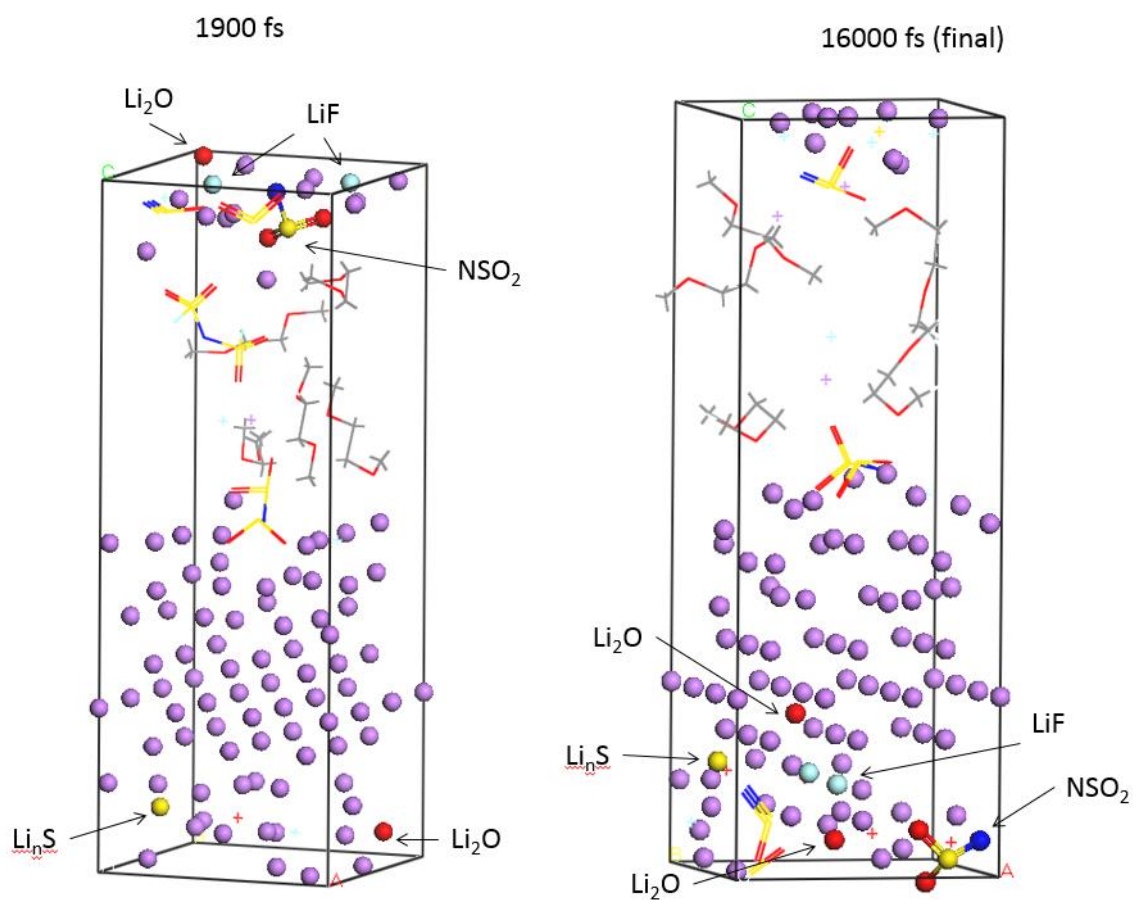


**Figure 44.** Left: DME, 4M LiFSI, at 1.9 ps, highlighting molecule 2. Right: After 16.0 ps. Color key: red, oxygen; white, hydrogen; blue, nitrogen; purple, lithium; yellow, sulfur; grey, carbon; teal, fluorine

For LiFSI molecule 3, the charge analysis results are seen below in Figure 45.

3

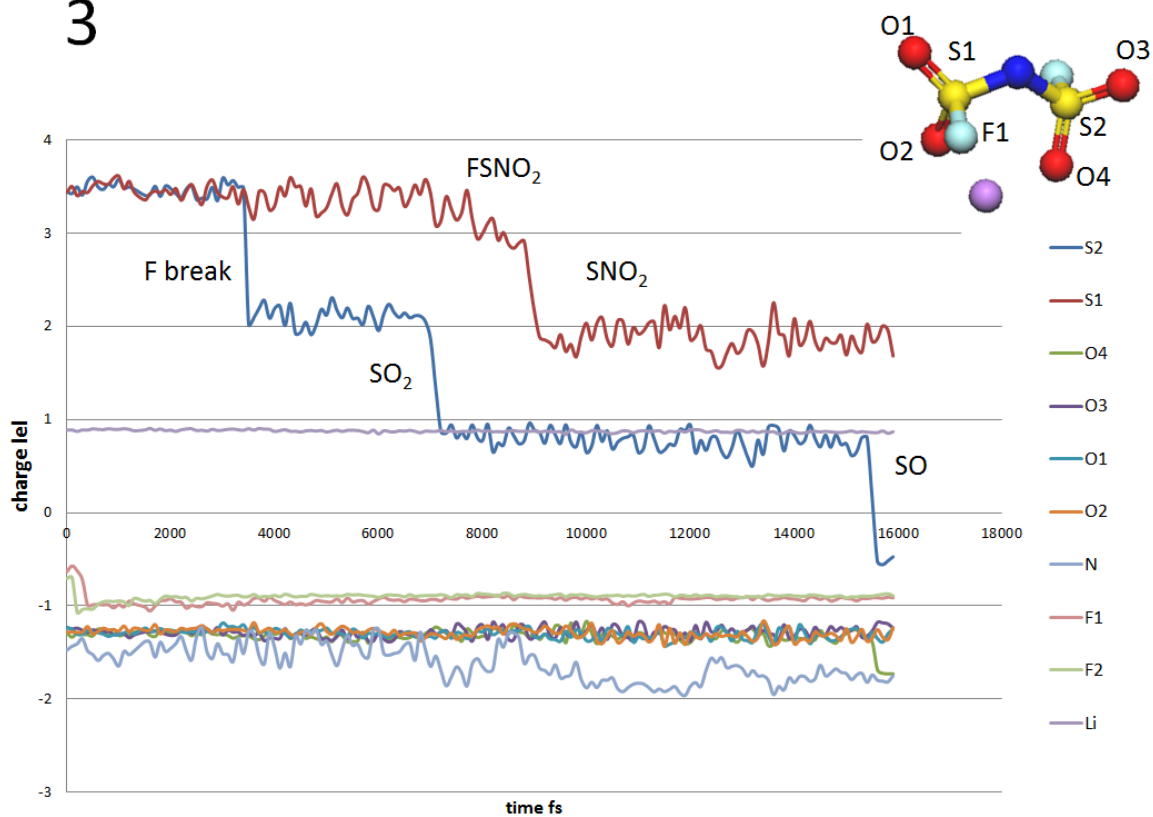
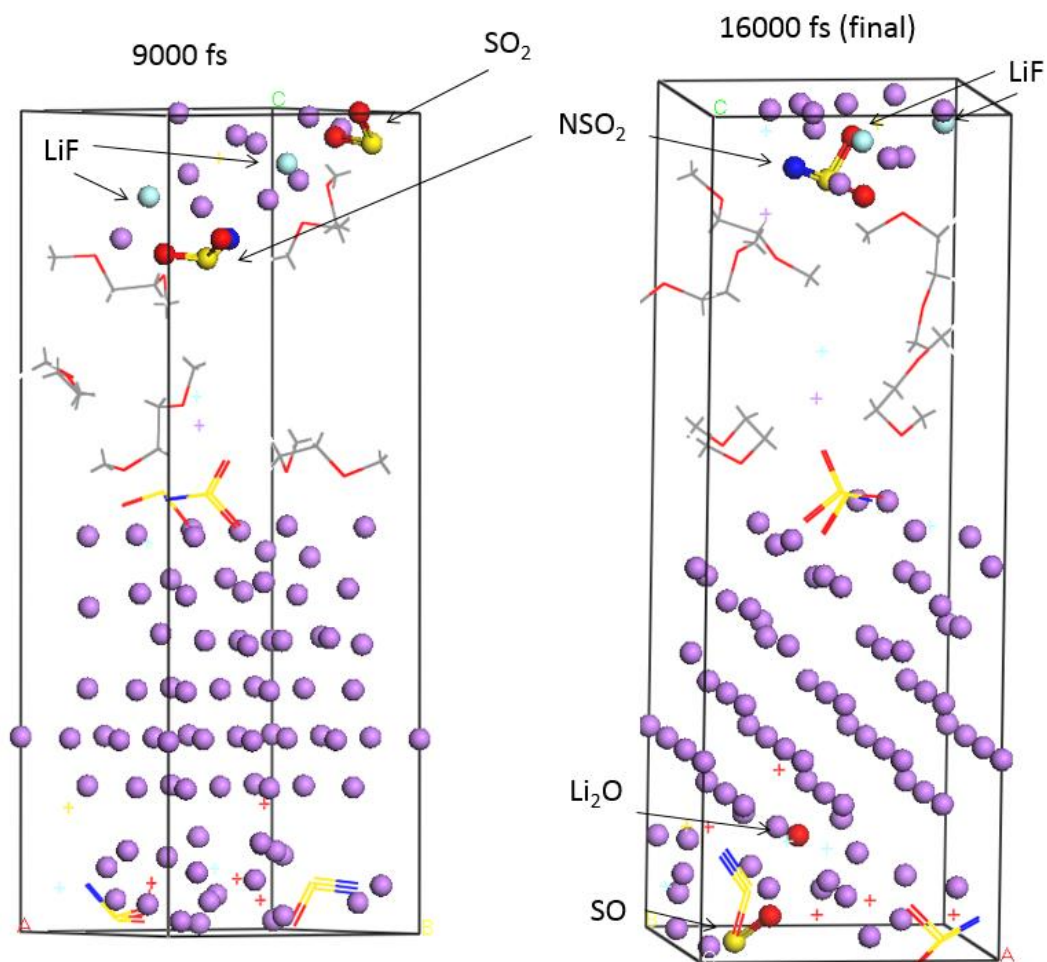


Figure 45. Charge analysis results for molecule 3

Reactions of molecule 3 are shown in Figure 46 below.



**Figure 46.** Left: DME, 4M LiFSI, at 9.0 ps, highlighting molecule 3. Right: After 16.0 ps. Color key: red, oxygen; white, hydrogen; blue, nitrogen; purple, lithium; yellow, sulfur; grey, carbon; teal, fluorine

For LiFSI molecule 4, the charge analysis results are seen below in Figure 47, with the reactions followed in Figure 48.

4

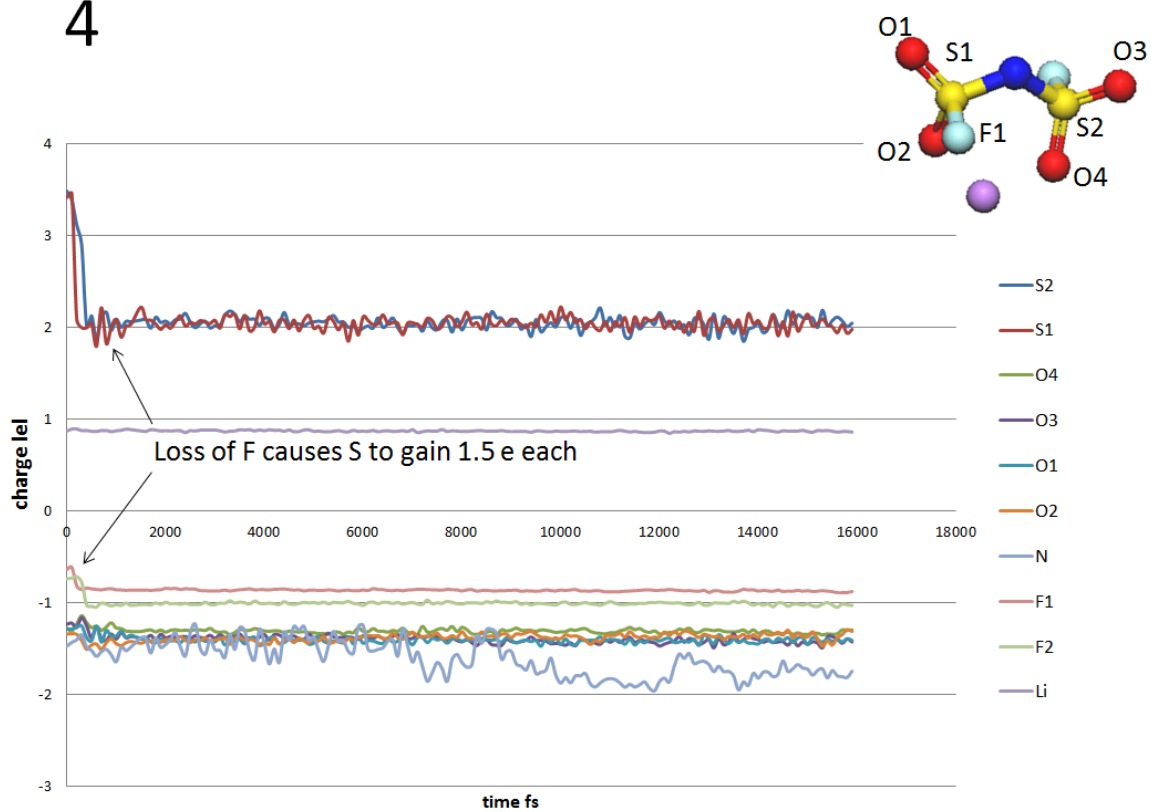
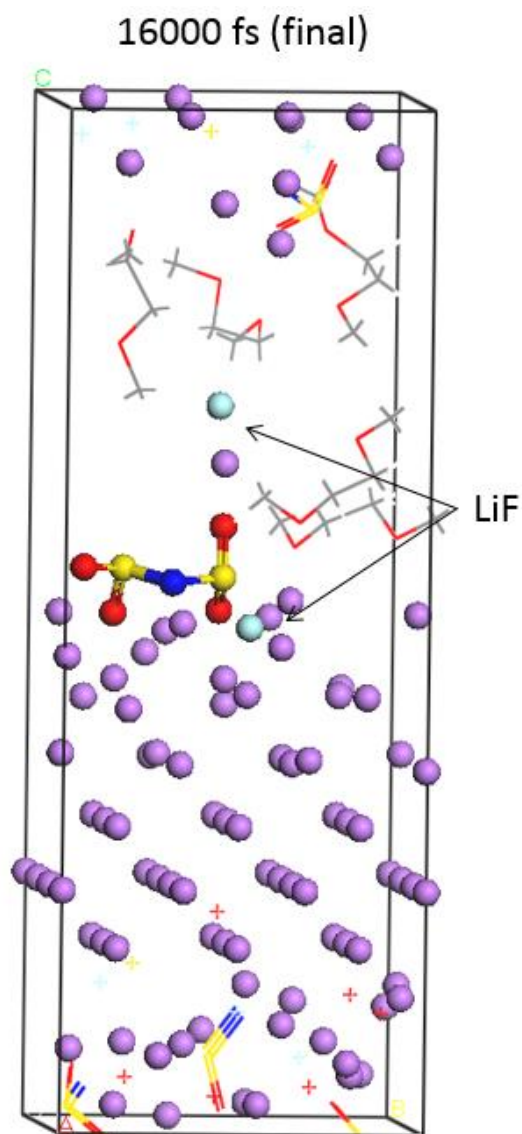


Figure 47. Charge analysis results for molecule 4



**Figure 48.** DME, 4M LiFSI, at 16.0 ps, highlighting molecule 4. Color key: red, oxygen; white, hydrogen; blue, nitrogen; purple, lithium; yellow, sulfur; grey, carbon; teal, fluorine

From these results, we are able to draw a few conclusions about the behavior of the LiFSI salt near the lithium anode. First, dissociation of the salt seems to catalyze the rest of the salt decomposition. Upon delithiation, the molecule is much more prone to fragmenting, and the delithiation reaction often occurs simultaneously with

defluorination. But perhaps the biggest takeaway from these high molarity LiFSI simulations is that the salt is relatively stable away from the anode surface, and that decomposition at the surface requires the proper environment and orientation. Consider that LiFSI molecule 4 undergoes almost no decomposition despite being the salt molecule closest to the anode at the start of simulation. Molecule 1, however, is oriented with the lithium nearest to the anode surface, and it reacts almost instantaneously and quite extensively. In order to establish an energetic understanding of these reactions, DFT energy calculations were performed in Gaussian to establish reaction energies and thermodynamic favorabilities based the direction of lithium attack on the salt molecule. Neutral LiFSI molecules were simulated, as were charged and uncharged lithium atoms, and then these two species were combined with the charged or neutral lithium either beneath the plane of the ring, in-plane and near the nitrogen (behind), or in-plane and near the lithium (front), as shown in Figure 49.



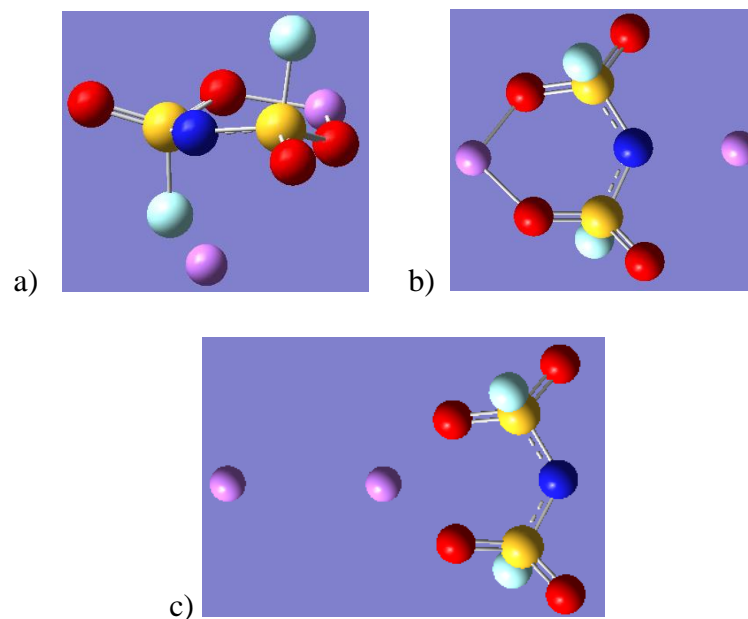


**Figure 49.** Direction of lithium attack. (a) Below. (b) Behind. (c) Front. Color key: red, oxygen; blue, nitrogen; purple, lithium; yellow, sulfur; teal, fluorine

The energetic results of these orientations are seen in Figure 50.

Reaction (Front)	Reaction E [eV]	Reaction G [eV]
LiFSI + Li <sup>0</sup>	-0.343	-0.163
LiFSI + Li <sup>1</sup>	-0.091	0.177

Reaction (Below)	Reaction E [eV]	Reaction G [eV]
LiFSI + Li <sup>0</sup>	-3.155	-2.863
LiFSI + Li <sup>1</sup>	-0.163	0.168

Reaction (Front)	Reaction E [eV]	Reaction G [eV]
LiFSI + Li <sup>0</sup>	-2.796	-2.521
LiFSI + Li <sup>1</sup>	-0.193	0.084

**Figure 50.** Reaction energies at various lithium orientations.

This data seems to indicate that the lithium attack from the “below” position is the most favorable, but this seems to conflict with what we see in the AIMD results. Below in Figure 51 is the optimized structure for the reaction of LiFSI and Li<sup>0</sup> from the “below” position.

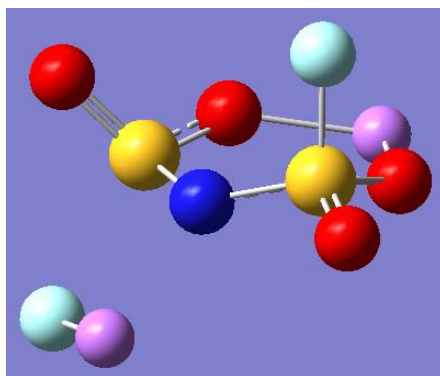


**Figure 51.** Optimized structure of below  $\text{Li}^0$  attack. Color key: red, oxygen; blue, nitrogen; purple, lithium; yellow, sulfur; teal, fluorine

We can easily see that for this configuration, a reaction has actually taken place – the very same reaction seen in the AIMD simulation. The attacking lithium atom has removed a fluorine atom and formed LiF, which seems to be stabilized by the rest of the salt molecule. This reaction is extremely favorable, as might be expected. Table 5 shows the energetics of LiF formation from both charged and neutral species.

**Table 5.** LiF formation energetics

Solvent	Reaction E [eV]	Reaction G [eV]
$\text{Li}^0 + \text{F}^0$	-1.485	-1.285
$\text{Li}^1 + \text{F}^{-1}$	-6.708	-6.474

From these results, it appears that the favorability seen in Figure 50 for the lithium attack from below comes in large part from the favorability of the formation of LiF.

This data seems to support the results of the previous AIMD simulation; we see that the “front” position of lithium attack is actually very thermodynamically favorable, while the “below” position is much less so. This provides us a solid theoretical explanation for the difference in stability of molecules 1 and 4 in the 4M LiFSI simulation. Also, we see that attack by neutral lithium is much more effective than charged, even when near nucleophilic sites, such as the nitrogen in the “behind” configuration.

In summary, while we did not see the same coordination effect noted by Qian et al. (salt molecules aligning and forming a network in the electrolyte), we were able to observe some very intriguing behavior of the LiFSI molecules and their interactions with the lithium surface. The formation of an SEI at the anode surface was observed, and this occurs both more quickly and completely for the LiFSI salt versus the LiTFSI. Several products of the LiFSI decomposition over a 16 ps timeframe were also observed, along with the changes in charge experienced by the individual atoms of each salt molecule.

Additionally, several positive attributes of this salt as compared to LiTFSI were found. The lower MW of the LiFSI means that a higher amount of lithium is present within each mole of salt, and therefore the electrolyte, at the start of the simulation, something that will only help the cell’s energy density and performance. Also, delithiation seems to be the most favorable method of salt decomposition at the anode, meaning that the salt can positively contribute to lithium cycling without decomposition. This could result in the formation of a coordinated network of salt molecules capable of both allowing faster lithium diffusion away from the anode surface and acting as a

barrier to any long-chain PS species which might otherwise migrate to the surface. This beneficial SEI could be the driving factor in the improved performance reported for high-molarity LiFSI cells.

## CHAPTER V

### SUMMARY

In this thesis, we have examined a wide variety of lithium-sulfur anode components which have the potential to dramatically impact the overall cell performance. The lithium crystal structure was investigated, with mixtures of solvent molecules at both the (100) and (110) planes undergoing AIMD simulations. From these results, it was determined that for these two cases, the crystal structure has a minimal effect on solvent stability, with the (110) case indicating the potential for slightly more EC compatibility. However, due to the apparent instability of this crystal structure, the stability of DOL and DME near both planes, and the desire for compatibility with the results of other researchers within the group, the (100) plane was chosen to undergo further testing.

The effects of electrolyte components on both the lithium surface and solvent stability were investigated, and it was found that for all binary solvent systems, the addition of the LiTFSI salt had no significant impact on solvent stability, and that the salt itself was quite prone to decomposition, even away from the anode surface. Next, the addition of polysulfides at various concentrations was studied, and it was found that PS decomposition occurs almost instantaneously, even in the bulk electrolyte. These fragments tend to diffuse toward the anode surface to form an amorphous layer of  $\text{Li}_2\text{S}$ , and in the case of high molarity PS mixtures, the bulk PS decomposition products are even capable of drawing lithium atoms upward from the surface. While the presence of

PS does not seem to catalyze solvent decomposition, it does seem to stabilize the LiTFSI salt by helping to passivate the anode surface. No distinction was found between the ring and linear initial PS configurations.

D2 was shown to be a viable solvent for use in this environment, as it proved relatively stable near the anode in addition to driving the PS decomposition fragments into the bulk lithium crystal. The fluorine atoms from the D2 decomposition remain near the surface, with the potential to hamper further PS shuttle as reported in literature.<sup>15</sup> Finally, the employment of an alternative salt, LiFSI, was examined. While AIMD showed less stability for it near the anode, as compared to the LiTFSI, DFT calculations indicated the reactivity of both species is very similar, and that neither is favorable in DME alone.

To further explore the effects of the LiFSI salt, a study of high molarity salt effects was conducted for the same 1:1 v/v DOL/DME, Li (100) system considered in the previous LiFSI simulations. The results showed that the salt molecule is less stable than LiTFSI for the same conditions, but that the LiFSI is more prone to delithiation and is stable away from the anode surface and even near the surface for certain orientations. The SEI formed by the LiFSI decomposition is reported to lead to positive effects on the cell performance, and while no bulk coordination of the salt was seen for this volume of electrolyte, the behavior of the LiFSI molecules seems to confirm previous experimental observations.<sup>25</sup>

In conclusion, this thesis has examined the impact of a bevy of factors which influence the performance of lithium-sulfur batteries. Using AIMD simulations, in

conjunction with static DFT optimizations, Bader charge analysis, and additional analytical techniques, we have gained insight into the inner machinations of crystal structure, electrolyte, and high molarity salt effects occurring at the lithium anode surface. It is the hope of this author that a deeper theoretical understanding of the way this system behaves will allow real-world Li-S systems to be better engineered to meet and overcome the challenges facing the commercialization of this technology.



## REFERENCES

1. Wu, H.; Cui, Y., Designing Nanostructured Si Anodes for High Energy Lithium Ion Batteries. *Nano Today* **2012**, *7*, 414-429.
2. Ostadhosseini, A.; Cubuk, E. D.; Tritsarlis, G. A.; Kaxiras, E.; Zhang, S.; van Duin, A. C. T., Stress Effects on the Initial Lithiation of Crystalline Silicon Nanowires: Reactive Molecular Dynamics Simulations Using Reaxff. *Physical Chemistry Chemical Physics* **2015**, *17*, 3832-3840.
3. Scrosati, B.; Garche, J., Lithium Batteries: Status, Prospects and Future. *Journal of Power Sources* **2010**, *195*, 2419-2430.
4. Larcher, D.; Beattie, S.; Morcrette, M.; Edstroem, K.; Jumas, J.-C.; Tarascon, J.-M., Recent Findings and Prospects in the Field of Pure Metals as Negative Electrodes for Li-Ion Batteries. *Journal of Materials Chemistry* **2007**, *17*, 3759-3772.
5. Christensen, J.; Newman, J., A Mathematical Model of Stress Generation and Fracture in Lithium Manganese Oxide. *J. Electrochem. Soc.* **2006**, *153*, A1019-A1030.
6. Qi, Y.; Guo, H.; Hector, L. G., Jr.; Timmons, A., Threefold Increase in the Young's Modulus of Graphite Negative Electrode During Lithium Intercalation. *Journal of the Electrochemical Society* **2010**, *157*, A558-A566.
7. Beaulieu, L. Y.; Hatchard, T. D.; Bonakdarpour, A.; Fleischauer, M. D.; Dahn, J. R., Reaction of Li with Alloy Thin Films Studied by in Situ AFM. *J. Electrochem. Soc.* **2003**, *150*, A1457-A1464.
8. Li, J.; Dozier, A. K.; Li, Y.; Yang, F.; Cheng, Y.-T., Crack Pattern Formation in Thin Film Lithium-Ion Battery Electrodes. *J. Electrochem. Soc.* **2011**, *158*, A689-A694.
9. Congress, G. C. Li-S Company Sion Power Raises \$50m. <http://www.greencarcongress.com/2011/12/sion-20111227.html>.
10. Zheng, J.; Gu, M.; Wang, C.; Zuo, P.; Koech, P. K.; Zhang, J.-G.; Liu, J.; Xiao, J., Controlled Nucleation and Growth Process of  $\text{Li}_2\text{S}_2/\text{Li}_2\text{S}$  in Lithium-Sulfur Batteries. *Journal of the Electrochemical Society* **2013**, *160*, A1992-A1996.
11. Scheers, J.; Fantini, S.; Johansson, P., A Review of Electrolytes for Lithium-Sulphur Batteries. *Journal of Power Sources* **2014**, *255*, 204-218.

12. Cuisinier, M.; Cabelguen, P.-E.; Evers, S.; He, G.; Kolbeck, M.; Garsuch, A.; Bolin, T.; Balasubramanian, M.; Nazar, L. F., Sulfur Speciation in Li-S Batteries Determined by Operando X-Ray Absorption Spectroscopy. *Journal of Physical Chemistry Letters* **2013**, *4*, 3227-3232.
13. Yang, Y.; Zheng, G.; Cui, Y., Nanostructured Sulfur Cathodes. *Chemical Society Reviews* **2013**, *42*, 3018-3032.
14. Christensen, J.; Newman, J., Stress Generation and Fracture in Lithium Insertion Materials. *Journal of Solid State Electrochemistry* **2006**, *10*, 293-319.
15. Weng, W.; Pol, V. G.; Amine, K., Ultrasound Assisted Design of Sulfur/Carbon Cathodes with Partially Fluorinated Ether Electrolytes for Highly Efficient Li/S Batteries. *Advanced Materials* **2013**, *25*, 1608-1615.
16. Diao, Y.; Xie, K.; Xiong, S.; Hong, X., Insights into Li-S Battery Cathode Capacity Fading Mechanisms: Irreversible Oxidation of Active Mass During Cycling. *Journal of the Electrochemical Society* **2012**, *159*, A1816-A1821.
17. Bruce, P. G.; Freunberger, S. A.; Hardwick, L. J.; Tarascon, J.-M., LiO<sub>2</sub> and Li-S Batteries with High Energy Storage. *Nature Materials* **2012**, *11*, 19-29.
18. Chen, Y.-X.; Kaghazchi, P., Metalization of Li<sub>2</sub>S Particle Surfaces in Li-S Batteries. *Nanoscale* **2014**, *6*, 13391-13395.
19. Schneider, H., et al., On the Electrode Potentials in Lithium-Sulfur Batteries and Their Solvent-Dependence. *Journal of the Electrochemical Society* **2014**, *161*, A1399-A1406.
20. Hofmann, A. F.; Fronczek, D. N.; Bessler, W. G., Mechanistic Modeling of Polysulfide Shuttle and Capacity Loss in Lithium-Sulfur Batteries. *Journal of Power Sources* **2014**, *259*, 300-310.
21. Choi, J.-H.; Lee, C.-L.; Park, K.-S.; Jo, S.-M.; Lim, D.-S.; Kim, I.-D., Sulfur-Impregnated MWCNT Microball Cathode for Li-S Batteries. *Rsc Advances* **2014**, *4*, 16062-16066.
22. Huang, C., et al., Manipulating Surface Reactions in Lithium-Sulphur Batteries Using Hybrid Anode Structures. *Nature Communications* **2014**, *5*.
23. Leung, K.; Rempe, S. B.; Foster, M. E.; Ma, Y.; del la Hoz, J. M. M.; Sai, N.; Balbuena, P. B., Modeling Electrochemical Decomposition of Fluoroethylene Carbonate on Silicon Anode Surfaces in Lithium Ion Batteries. *Journal of the Electrochemical Society* **2014**, *161*, A213-A221.

24. de la Hoz, J. M. M.; Soto, F. A.; Balbuena, P. B., Effect of the Electrolyte Composition on SEI Reactions at Si Anodes of Li-Ion Batteries. *Journal of Physical Chemistry C* **2015**, *119*, 7060-7068.
25. Qian, J.; Henderson, W. A.; Xu, W.; Bhattacharya, P.; Engelhard, M.; Borodin, O.; Zhang, J.-G., High Rate and Stable Cycling of Lithium Metal Anode. *Nature Communications* **2015**, *6*.
26. Anderson, M. S.; Swenson, C. A., Experimental Equations of State for Cesium and Lithium Metals to 20-Kbar and the High-Pressure Behavior of the Alkali-Metals. *Physical Review B* **1985**, *31*, 668-680.
27. Kresse, G., Ab-Initio Molecular-Dynamics for Liquid-Metals. *Journal of Non-Crystalline Solids* **1995**, *193*, 222-229.
28. Kresse, G.; Furthmuller, J., Efficiency of Ab-Initio Total Energy Calculations for Metals and Semiconductors Using a Plane-Wave Basis Set. *Computational Materials Science* **1996**, *6*, 15-50.
29. Perdew, J. P.; Chevary, J. A.; Vosko, S. H.; Jackson, K. A.; Pederson, M. R.; Singh, D. J.; Fiolhais, C., Atoms, Molecules, Solids, and Surfaces - Applications of the Generalized Gradient Approximation for Exchange and Correlation. *Physical Review B* **1992**, *46*, 6671-6687.
30. Blochl, P. E., Projector Augmented-Wave Method. *Physical Review B* **1994**, *50*, 17953-17979.
31. Perdew, J. P.; Burke, K.; Ernzerhof, M., Generalized Gradient Approximation Made Simple. *Physical Review Letters* **1996**, *77*, 3865-3868.
32. Sigma-Aldrich 1,3-Dioxolane.  
<http://www.sigmaaldrich.com/catalog/product/sial/184497?lang=en&region=US>.
33. Sigma-Aldrich 1,2-Dimethoxyethane.  
<http://www.sigmaaldrich.com/catalog/product/sial/e27408?lang=en&region=US>.
34. Sigma-Aldrich Ethylene Carbonate.  
<http://www.sigmaaldrich.com/catalog/product/aldrich/e26258?lang=en&region=US>.
35. Synquest Laboratories 1,1,2,2-Tetrafluoroethyl 2,2,3,3-Tetrafluoropropyl Ether.  
<http://www.synquestlabs.com/product/id/22001.html>.
36. Park, M. S.; Ma, S. B.; Lee, D. J.; Im, D.; Doo, S.-G.; Yamamoto, O., A Highly Reversible Lithium Metal Anode. *Scientific Reports* **2014**, *4*.

37. Andersson, A. M.; Herstedt, M.; Bishop, A. G.; Edstrom, K., The Influence of Lithium Salt on the Interfacial Reactions Controlling the Thermal Stability of Graphite Anodes. *Electrochimica Acta* **2002**, *47*, 1885-1898.
38. Agostini, M.; Scrosati, B.; Hassoun, J., An Advanced Lithium-Ion Sulfur Battery for High Energy Storage. *Advanced Energy Materials* **2015**, *5*.
39. Xu, R., et al., Insight into Sulfur Reactions in Li-S Batteries. *Acs Applied Materials & Interfaces* **2014**, *6*, 21938-21945.
40. Vijayakumar, M., et al., Molecular Structure and Stability of Dissolved Lithium Polysulfide Species. *Physical Chemistry Chemical Physics* **2014**, *16*, 10923-10932.
41. Barchasz, C.; Molton, F.; Duboc, C.; Lepretre, J.-C.; Patoux, S.; Alloin, F., Lithium/Sulfur Cell Discharge Mechanism: An Original Approach for Intermediate Species Identification. *Analytical Chemistry* **2012**, *84*, 3973-3980.
42. Mikhaylik, Y. V.; Akridge, J. R., Polysulfide Shuttle Study in the Li/S Battery System. *Journal of the Electrochemical Society* **2004**, *151*, A1969-A1976.
43. Moy, D.; Manivannan, A.; Narayanan, S. R., Direct Measurement of Polysulfide Shuttle Current: A Window into Understanding the Performance of Lithium-Sulfur Cells. *Journal of the Electrochemical Society* **2015**, *162*, A1-A7.
44. Assary, R. S.; Curtiss, L. A.; Moore, J. S., Toward a Molecular Understanding of Energetics in Li-S Batteries Using Nonaqueous Electrolytes: A High-Level Quantum Chemical Study. *Journal of Physical Chemistry C* **2014**, *118*, 11545-11558.
45. Steudel, Y.; Wong, M. W.; Steudel, R., Electrophilic Attack on Sulfur-Sulfur Bonds: Coordination of Lithium Cations to Sulfur-Rich Molecules Studied by Ab Initio Mo Methods. *Chemistry-a European Journal* **2005**, *11*, 1281-1293.
46. Azimi, N.; Weng, W.; Takoudis, C.; Zhang, Z., Improved Performance of Lithium-Sulfur Battery with Fluorinated Electrolyte. *Electrochemistry Communications* **2013**, *37*, 96-99.
47. Eshetu, G. G.; Grugeon, S.; Gachot, G.; Mathiron, D.; Armand, M.; Laruelle, S., LiFSI vs. LiPF<sub>6</sub> Electrolytes in Contact with Lithiated Graphite: Comparing Thermal Stabilities and Identification of Specific Sei-Reinforcing Additives. *Electrochimica Acta* **2013**, *102*, 133-141.
48. Philippe, B.; Dedryvere, R.; Gorgoi, M.; Rensmo, H.; Gonbeau, D.; Edstrom, K., Improved Performances of Nanosilicon Electrodes Using the Salt LiFSI: A

Photoelectron Spectroscopy Study. *Journal of the American Chemical Society* **2013**, *135*, 9829-9842.